Determining ULF Wave Contributions to Geomagnetically Induced Currents: The Important Role of Sampling Rate

Michael D. Hartinger[1], Xueling Shi[2,3], Craig J. Rodger[4], Ikuko Fujii[5], E. Joshua Rigler[6], Karl Kappler[1], Jürgen Matzka[7], Jeffrey J. Love[6], Joseph B.H. Baker[2], Daniel H. Mac Manus[4], Michael Dalzell[8], Tanja Petersen[9]

,

[1]Space Science Institute, Boulder, CO, USA.
[2]Department of Electrical and Computer Engineering, Virginia Tech, Blacksburg, VA, USA.
[3]High Altitude Observatory, National Center for Atmospheric Research, Boulder, CO, USA.
[4]Department of Physics, University of Otago, Dunedin, New Zealand
[5]Meteorological College, Japan Meteorological Agency, Kashiwa, Chiba, Japan
[6]U.S. Geological Survey, Geomagnetism Program, Golden, CO, USA
[7]GFZ German Research Center for Geosciences, Potsdam, Germany
[8]Transpower New Zealand Limited, Wellington, New Zealand
[9]GNS Science, Lower Hutt, New Zealand

Key Points:

- Waves with periods $<\sim$ 2 minutes occur at magnetic latitudes $< 60^\circ$ throughout the 29-31 October 2003 storm
- The waves drive or contribute significantly to geomagnetically induced currents that are comparable to 14-year peak values
- 0.1-1.0 Hz sampling rates are required to determine wave contributions to currents at magnetic latitudes < 60 degrees

Corresponding author: Michael Hartinger, `mhartinger@spacescience.org`

Abstract

Past studies found that large-amplitude geomagnetically induced current (GIC) related to magnetospheric Ultra Low Frequency (ULF) waves tend to be associated with periods > 120 s at magnetic latitudes > 60 degrees, with comparatively (1) smaller GIC amplitudes at lower latitudes and shorter wave periods and (2) fewer reports of waves associated with GIC at lower latitudes. ULF wave periods generally decrease with decreasing latitude; thus, we examine whether these trends might be due, in part, to the undersampling of ULF wave fields in commonly available measurements with 60 s sampling intervals. We use geomagnetic field (**B**), geoelectric field (**E**), and GIC measurements with 0.5-10 s sampling intervals during the 29-31 October 2003 geomagnetic storm to show that waves with periods $<\sim$ 120 s were present during times with the largest amplitude **E** and GIC variations. These waves contributed to roughly half the maximum **E** and GIC values, including during times with the maximum GIC values reported over a 14-year monitoring interval in New Zealand. The undersampling of wave periods < 120 s in 60 s measurements can preclude identification of the cause of the GIC during some time intervals. These results indicate (1) ULF waves with periods ≤ 120 s are an important contributor to large amplitude GIC variations, (2) the use of 0.1-1.0 Hz sampling rates reveals their contributions to **B**, **E**, and GIC, and (3) these waves' contributions are likely strongest at magnetic latitudes < 60 degrees where ULF waves often have periods < 120 s.

Plain Language Summary

Geomagnetic field variation can induce geoelectric fields in the Earth that interfere with the operation of grounded electric power transmission systems. There are many sources of geomagnetic field variation, including plasma waves in the near-Earth space environment. Past studies have found that wave periods between 120-600 s in high latitude regions led to the largest electrical currents in power systems. The waves responsible for driving these electrical currents have periods that decrease with decreasing latitude. We examine whether these trends may be partly due to the wide use of measurements with sampling rates that cannot resolve wave periods below 120 s. We use measurements sampled every 0.5-10 s during a major geomagnetic storm to show that wave periods shorter than 120 s can drive large amplitude geoelectric field and electrical current variations. These results suggest (1) waves with periods < 120 s are an important contributor to electrical currents in power systems, (2) the use of sampling intervals of 1-10 s reveals their contributions, and (3) these waves' contributions are likely strongest at middle and low latitude regions where wave periods are often < 120 s.

1 Introduction

Geomagnetic field (**B**) variations induce geoelectric field (**E**) variations in the Earth. These **E** variations are capable of driving damaging geomagnetically induced currents (GIC) in, for example, power grids, gas and oil pipelines, and telecommunications cables (e.g., Thomson, 2007; Pulkkinen et al., 2017; Pilipenko, 2021). It is widely recognized that **E** is the crucial link between magnetosphere-ionosphere current systems and GIC (Pulkkinen et al., 2017); thus, many recent studies have focused on characterizing **E** (Kelbert et al., 2017; Love et al., 2019; Lucas et al., 2018, 2020), which depends both on **B** and the electrical conductivity of the Earth.

Several studies have explored the impact of **B** sampling rate on estimates of extreme **E** values and GIC modeling, with mixed results. Some studies found that sampling intervals of 60 s can adequately capture **B**/**E**/GIC variations (e.g., Pulkkinen et al., 2006), while others (e.g., Grawe et al., 2018; Grawe & Makela, 2021; Trichtchenko, 2021) found that 60 s measurements are not adequate due to the presence of variations with frequencies (f) higher than the Nyquist frequency ($f_{Nyquist60} = 0.0083$ Hz for mea-

surements sampled every 60 s). Rogers et al. (2021) found for three locations in the United Kingdom that **B** fluctuations with roughly 1200 s period ($f << f_{Nyquist60}$) produced the most intense **E** when considering events occurring several times per year, whereas the 1-in-100 year return levels were greatest for 30-120 s period fluctuations ($f \geq f_{Nyquist60}$). Trichtchenko (2021) found that a 0.1 Hz sampling rate is generally needed to understand power system responses and posed the question, "What should be the sampling rate (or Nyquist frequency) in order to provide an adequate representation of the fast geomagnetic variations (such as storm sudden commencement (SSC), substorms, pulsations, and rapid variations during the main phase of the storm) for use in the calculations of the extreme geoelectric field values and in the GIC modeling?" Motivated by this question, the present study will focus on the recommended sampling rate for one particular source of **B** listed by Trichtchenko (2021), pulsations, considering several factors: expected pulsation frequencies, the amplitude of **B**/**E** related to pulsations at different frequencies, and the ability of pulsations to cause potentially hazardous GIC. Pulsations and other sources of fast geomagnetic variations (e.g., SSCs, substorms) are not mutually exclusive and can occur at the same time. We return to this point in later sections, particularly section 3.

Pulsations are also known as Ultra Low Frequency (ULF) waves (Orr, 1973; McPherron, 2005), with ULF being a frequency designation for magnetospheric plasma waves ranging from 0.001-5 Hz (Jacobs et al., 1964). Hereafter, we only use the term "ULF waves." At the lower end of the ULF band, waves are usually well-described by an ideal magnetohydrodynamic (MHD) approximation (Southwood & Hughes, 1983). The bounded, inhomogeneous medium of the Earth's magnetosphere supports a variety of MHD modes analogous to standing waves:

1. Standing Alfvén waves: These are analogous to waves on a string where the natural frequency of the wave depends on the length of the magnetic field line and wave speed (Sugiura & Wilson, 1964). The frequencies of these waves vary with magnetic latitude, generally increasing in frequency as magnetic latitude decreases. Standing Alfvén waves can be observed at magnetic latitudes corresponding to closed magnetic field lines and in all geomagnetic conditions. The fundamental frequency varies depending on several factors including geomagnetic latitude, geomagnetic activity, and local time (Takahashi & Anderson, 1992; Wild et al., 2005).
2. Trapped/Partially trapped magnetosonic waves: Magnetosonic waves can become partly radially trapped between various boundaries in the magnetosphere, with their frequencies related to the wave speeds and the size of the region in which they are trapped. These wave modes include cavity modes, waveguide modes, and virtual resonances (Wright & Mann, 2006; Lee & Takahashi, 2006). They can be observed at a wide range of magnetic latitudes during all geomagnetic conditions (Keiling & Takahashi, 2011). The wave period does not change with latitude, and the same period can be observed at a wide range of latitudes and local times (e.g., Pilipenko et al., 2010; Shi et al., 2017; Hartinger et al., 2017). The plasmasphere region has frequently been linked to wave trapping, with theory, modeling, and observation confirming the typical fundamental plasmaspheric cavity mode/virtual resonance frequency is in the ∼0.007-0.022 Hz range (Keiling & Takahashi, 2011; Shi et al., 2017; Hartinger et al., 2017; Takahashi et al., 2018); these plasmaspheric waves are most often observed at magnetic latitudes ∼<60 degrees.

These two broad standing wave categories can occur simultaneously. For example, Takahashi et al. (2018) showed observations and numerical simulations of a cavity mode driven by a solar wind pressure pulse that, in turn, feeds energy into standing Alfvén waves via a process known as field line resonance (Tamao, 1965; Glassmeier et al., 1999). Figure 1 shows typical frequencies for these different wave modes based on past observations, including during the 29-31 October 2003 storm (Takasaki et al., 2006; Kale et al., 2009; Marin et al., 2014) and similar conditions such as the aftermath of interplanetary shocks/SSC

(Takahashi et al., 2018). As seen in Figure 1, both plasmaspheric virtual resonance/cavity modes and standing Alfvén waves are undersampled in studies relying on measurements sampled every 60 s at magnetic latitudes <∼60 degrees, as their typical frequencies are >∼ $f_{Nyquist60}$.

Past studies have linked ULF waves to **B** (see above), **E** (e.g., Heyns et al., 2021; Hartinger et al., 2020; Shi, Hartinger, et al., 2022), and GIC variations (e.g., Pulkkinen et al., 2006; Viljanen et al., 2006; Belakhovsky et al., 2019; Yagova et al., 2021). These studies have generally found that the largest ULF wave **B** and GIC amplitudes are observed at magnetic latitudes >∼60 degrees for waves with $f < f_{Nyquist60}$ (Pilipenko, 2021). Several studies have been conducted at magnetic latitudes >∼60 degrees using measurements from the Kola peninsula in Russia (e.g., Belakhovsky et al., 2019; Apatenkov et al., 2020; Yagova et al., 2021), where waves with $f < f_{Nyquist60}$ drive the largest amplitude GIC, in some cases as large as ∼100 A. Additional studies have examined GIC in gas pipelines at magnetic latitudes near 60 degrees, with the largest amplitude GIC often originating from waves with $f < f_{Nyquist60}$ (Pulkkinen & Kataoka, 2006). Based on these past observations, in particular the tendency for larger wave amplitudes and larger GIC for $f < f_{Nyquist60}$, a few studies have recently suggested that waves with periods of 120-600 s drive the most intense GIC (Pilipenko, 2021; Yagova et al., 2021).

Reasons to further explore whether this tendency for smaller **B** and GIC for waves with $f > f_{Nyquist60}$ generalizes to magnetic latitudes < 60 degrees include:

1. There are limited **B** measurements with sampling intervals less than 60 s, particularly during historical geomagnetic storms or long monitoring intervals (Trichtchenko, 2021). Thus, extreme ULF wave **B** amplitudes for wave $f > f_{Nyquist60}$ are not as well constrained as for $f < f_{Nyquist60}$.
2. As shown in Figure 1, several categories of ULF waves are undersampled when using 60 s measurements at magnetic latitudes < 60 degrees. Since their frequency content is concentrated in a narrow frequency band, they will be removed from time series that have been low-pass filtered and resampled to obtain 60 s measurements. In contrast, waves with $f < f_{Nyquist60}$ and other phenomena with a broadband frequency spectrum are fully or partially retained in 60 s data.
3. Case studies, such as the 24 March 1991 SSC, show the tendency for larger amplitude **B** and **E** variations at $f < f_{Nyquist60}$ does not always apply to magnetic latitudes < 60 degrees. During this event, waves with $f >\sim f_{Nyquist60}$ were observed globally with **B** amplitudes of ∼100-200 nT (Yumoto et al., 1994; Araki et al., 1997, Figure 5a). Concerning GIC, Kappenman (2003) presented measurements following an SSC of damped, sinusoidal GIC at multiple locations in the United States power grid (Western Virginia, New York) with initial amplitudes ranging from 66 to 130A (Figures 2 and 3 in that study) and a wave $f >\sim f_{Nyquist60}$. According to Kappenman (2003), this SSC, "produced some of the largest GICs ever measured in the United States at midlatitude locations" (page 2 of Kappenman, 2003).

Motivated by these facts and past observations, we examine additional **B**, **E**, and GIC measurements at magnetic latitudes < 60 degrees and with sampling intervals less than 60 s during the 29-31 October 2003 geomagnetic storm (section 2). We examine these measurements as well as high-pass filtered measurements ($f >\sim f_{Nyquist60}$), low-pass filtered measurements ($f < f_{Nyquist60}$), and measurements with 60 s sampling intervals, comparing maximum and minimum values in the time rate of change of **B**, **E**, and GIC. We further determine whether ULF waves are present during periods with maximum/minimum **E** and GIC values using standard visual identification criteria (Jacobs et al., 1964). We show with examples that waves with $f >\sim f_{Nyquist60}$ drive or contribute significantly to **B**, **E**, and GIC variations with amplitudes comparable to the maximum values detected during extended monitoring intervals in Japan and New Zealand.

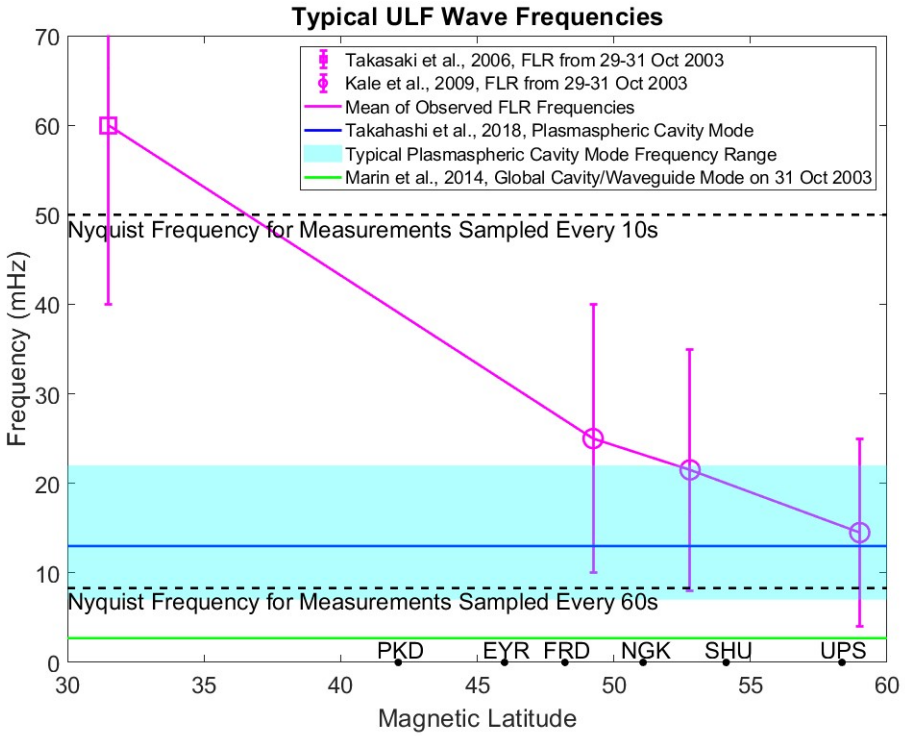

Figure 1. Frequencies for different ULF waves as a function of magnetic latitude, based on published observations from the 29-31 October 2003 storm and similar conditions. Pink circles and squares are for mean values for standing Alfvén wave frequencies (also commonly referred to as field line resonances, FLR) during the 29-31 October 2003 storm using observations from Kale et al. (2009) (Figure 3 of that study, YOR-CRK and NUR-OUJ pairs - comparable to a separate study at a different local time by Chi et al. (2005)) and Takasaki et al. (2006) (Figure 2 of that study); the bars are for the range of observed values during the 3-day interval. The green line is for an observed global waveguide mode on 31 October 2003 (Marin et al., 2014); the blue line is for an observed and simulated plasmaspheric cavity mode during an interplanetary shock event on 15 August 2015 (Takahashi et al., 2018); and the cyan shaded region is for a typical range of plasmaspheric cavity mode/virtual resonances based on review papers (Keiling & Takahashi, 2011) and wave transit time calculations (Takahashi et al., 2003, Figure 11). Dashed lines indicate the Nyquist frequencies for data sampled at 10 s and 60 s, while black circles on the bottom of the plot indicate the magnetic latitudes where most observations were collected for this study (see Table 1; the KAK station is at 28.99 degrees and not shown here).

In section 3, we use these results to justify a recommended sampling rate of 0.1-1.0 Hz for ULF waves. Finally, we summarize our results in section 4.

2 ULF B, E, and GIC during the 29-31 October 2003 storm

The 29-31 October 2003 geomagnetic storm, also known as the Halloween storm, was driven by two coronal mass ejections (CME). The first CME arrived at Earth on 29 October 2003 just after 0610 UT, and the other arrived on 30 October at 1600 UT; each resulted in an SSC (Balch et al., 2004). During the storm, there were numerous reports of GIC in power grids (Pulkkinen et al., 2005; Kappenman, 2005; Ngwira et al., 2008; Rodger et al., 2017; Heyns et al., 2021), gas pipelines (Viljanen et al., 2006), and oil pipelines (Hejda & Bochníček, 2005). For example, Heyns et al. (2021) examined South African GIC measurements with ULF wave GIC variations of ± 2-3 A for $0.002 < f < 0.022$ Hz variations, with somewhat larger amplitudes seen for lower frequency waves.

Several studies have examined **B** related to ULF waves during the 29-31 October 2003 storm, with significant attention paid to wave frequencies <∼0.004 Hz. Panasyuk et al. (2004), Potapov et al. (2006), Pilipenko et al. (2010), and Marin et al. (2014) examined wave activity during several phases of the storm, finding several time intervals with ∼0.003 Hz wave amplitudes of ∼100-300 nT at a wide range of magnetic latitudes and longitudes. Wave amplitudes were typically found to peak in the magnetic latitude range from 58 to 65 degrees, and the waves were associated with both standing Alfvén waves and global waveguide modes (Pilipenko et al., 2010). Love and Gannon (2010) observed similar period waves at low latitude stations during several intervals during the storm.

In this section, we present **B** (2.2), **E** (2.3), and GIC (2.4) measurements associated with ULF waves at magnetic latitudes < 60 degrees for several time intervals during the 29-31 October 2003 storm, placing them in context with extreme values obtained during extended monitoring intervals in Japan and New Zealand.

2.1 Datasets and Methodology

We use **B**, **E**, and GIC measurements from several regions around the world with measurements available at sampling rates ≥0.1 Hz. Station codes, coordinates, measurement type, and sampling rate are shown in Table 1 (see SI Figure S1 for a map). The geographic coordinates provided are in degrees north and degrees east. The geomagnetic (quasi-dipole) latitudes provided were obtained using the International Geomagnetic Reference Field (IGRF) model and calculator available from the British Geological Survey (Emmert et al., 2010) assuming a fractional year of 2003.8.

For the United States locations, we use **B** measurements from the United States Geological Survey (USGS) Geomagnetism Program sampled at 1.0 Hz (Love & Finn, 2011; Rigler & USGS Geomagnetism Program, 2023) at the Fredericksburg (FRD) and Shumagin (SHU) sites as well as **B** and **E** measurements from the University of California, Berkeley, Parkfield (PKD) monitoring site sampled at 1.0 Hz (Kappler et al., 2010).

Outside of the United States, we analyze **B** (Minamoto, 2013) and **E** (Fujii et al., 2015) measurements from the Kakioka Magnetic Observatory (KAK) station in Japan. These data are sampled at 1.0 Hz during the period of interest. Fujii et al. (2015) noted that unique ground conductivity structure near KAK tends to amplify the east-west component of **E** significantly relative to the north-south component at KAK, and relative to the east-west component at other nearby stations. Thus, we will not emphasize the amplitude of **E** variations at KAK relative to other locations, but rather the amplitudes observed at KAK during the 29-31 October 2003 storm relative to other intervals.

Table 1. Locations of Geomagnetic Field, Geoelectric Field, and GIC measurements used in this study. All parameters are relevant to the 29-31 October 2003 Geomagnetic Storm.

Network	Station	GEO Lat Degrees	GEO Lon Degrees	Quasi-Dipole Lat Degrees	Sampling Rate Hz	Type
USGS	FRD	38.20	-77.37	48.85	1.0	B
UC Berkeley	PKD	35.95	-120.5	41.47	1.0 1.0	B E
USGS	SHU	55.38	-160.5	52.96	1.0	B
GNS Science	EYR	-43.47	172.4	-50.04	0.2	B
Transpower NZ	ISL	-43.54	172.5	-50.09	0.2	GIC
Kakioka Mag. Obs.	KAK	36.23	140.2	28.99	1.0 1.0	B E
SGU	UPS	59.90	17.35	56.24	0.1	B
GFZ	NGK	52.07	12.66	47.85	2.0 1.0	B E

We also analyze measurements from two locations in Europe near southern Sweden, where GIC and power system disruptions were reported (e.g., Pulkkinen et al., 2005). In Sweden, we investigate **B** measurements from the IMAGE network (Tanskanen, 2009); specifically, **B** sampled at 0.1 Hz from the Uppsala (UPS) observatory in Sweden operated by the Geological Survey of Sweden (SGU). In Germany, we use **B** and **E** measurements from the German Research Centre for Geosciences (GFZ)-Potsdam Niemegk (NGK) observatory sampled at 2 Hz (**B**) and 1.0 Hz (**E**).

We further investigate **B** measurements from the South Island of New Zealand Eyrewell (EYR) observatory due to its long record of measurements sampled at >0.2 Hz and the availability of nearby GIC measurements. This site is operated by GNS Science. The highest sampling rate available from EYR has changed over time (Rodger et al., 2017). The 0.2 Hz data used in this study are frequently available throughout 2002, 2003, 2005, 2006-2009, and 2010; since 2011, 1.0 Hz data are routinely available.

We use GIC measurements from Transpower New Zealand Limited consisting of direct current (DC) measured in several transformers in the South Island of New Zealand. From 2001-2015, Hall effect current transducers (Liaisons Electroniques-Mécaniques [LEM] model LT 500 or LT 505-S) were used to collect these measurements (Marshall et al., 2012). These data were corrected to remove stray Earth return currents and calibration offsets, resulting in a nearly continuous set of GIC measurements from 2002-2019 (Mac Manus et al., 2017; Rodger et al., 2020). The sampling rate at which LEM DC current measurements are stored changes dynamically, with higher sampling rates used when the DC values are changing more rapidly (see the description in Clilverd et al., 2020). This means that GIC collected during geomagnetic storms and other active conditions have the highest sampling rate, 0.25 Hz, with lower sampling rates during periods with steady GIC. Data from the Islington (ISL) T6 transformer are used for this study as ISL is close to

the EYR magnetometer; the measurements at this transformer are referred to as ISL M6. For further details on the GIC dataset, see Mac Manus et al. (2017), Rodger et al. (2020), and Clilverd et al. (2020).

To facilitate comparison of **B** variations between time series with different baseline values, we subtract mean values corresponding to the time ranges shown in each figure. We also do this for **E** when comparing time intervals $\leq$ 20 minutes. To facilitate comparison of **E** variations when examining a longer 3-day time interval on 29-31 October 2003, we remove slowly varying trends in **E** unrelated to magnetosphere-ionosphere current systems by fitting a line (linear trend in time series) to each component of **E** and subtracting it from the original measurements; we fit the line using only the data collected on 29-31 October 2003. These procedures do not completely remove slowly varying sensor responses related to daily variations in air temperature and other factors unrelated to magnetosphere-ionosphere current systems (Fujii et al., 2015) which may be present in some of the measurements we analyze, but none of these factors affect our analysis or conclusions in this study; future work could remove these trends to study a wider frequency range (e.g., daily variations related to the solar quiet [Sq] current system). To show the relative contributions of **B**, **E**, and GIC variations with frequencies above and below $f_{Nyquist60}$, we apply digital high-pass and low-pass filters with 0.0083 Hz cutoff frequencies to these data in some figures. In particular, we use a forward-backward eighth order Butterworth filter constructed using the publicly available Python SciPy signal module ("butter" and "sosfiltfilt"). These filters are constructed to have a flat response in the pass band at frequencies near $f_{Nyquist60}$, thus providing more reliable estimates for maximum/minimum values during time intervals when variations have frequencies close to $f_{Nyquist60}$. The sum of the high-pass and low-pass filtered measurements also yields the original time series.

We use 60 s measurements to show how commonly available data that have frequently been used to study the 29-31 October 2003 storm and other historical storms differ from the 0.5-10 s samples obtained for this study. The 60 s data from FRD, EYR, KAK, UPS, and NGK are obtained from the INTERMAGNET database (Love & Chulliat, 2013; St. Louis, 2020); data from each site are processed using one of several different filter types and resampling methods to obtain the INTERMAGNET samples. For example, FRD and UPS sites use a Gaussian filter, while the KAK and NGK sites use a boxcar average. In some cases, the samples are centered at second 00 of the minute (e.g., KAK, UPS), whereas in other cases they are centered at 30 s (e.g., NGK). SHU and PKD are not available from INTERMAGNET for these dates, thus 60 s data are obtained for these sites via a 60 s boxcar average similar to that used for the KAK site and by SuperMAG (Gjerloev, 2012). The fact that different sites listed in Table 1 use different filters and resampling methods to obtain 60 s time series does not change our results, as all of the 60 s datasets are affected by the undersampling issues we discuss throughout this study. However, these different methods can result in different amplitudes for variations with frequencies near $f_{Nyquist60}$, and we briefly discuss these effects in later sections.

2.2 Geomagnetic Field Measurements

In this section, we review **B** measurements from several locations (see Table 1 and SI Figure S1) at magnetic latitudes < 60 degrees, including two time intervals during the 29-31 October 2003 storm that correspond to periods with ULF waves and with the largest ISL M6 GIC values during 14-year monitoring intervals. Figure 2 is for the horizontal magnitude of **B**, or H. In all panels, the black curves are for 0.5-10 s measurements (see Table 1 for sampling rate at each location); light gray curves are for 60 s measurements obtained from either INTERMAGNET (FRD, EYR, KAK, UPS, NGK) or by applying a centered boxcar average (PKD, SHU) as described in section 2.1; blue curves are for high-pass filtered measurements ($f > f_{Nyquist60}$); and red curves are for low-pass filtered measurements ($f < f_{Nyquist60}$). To emphasize amplitude differences be-

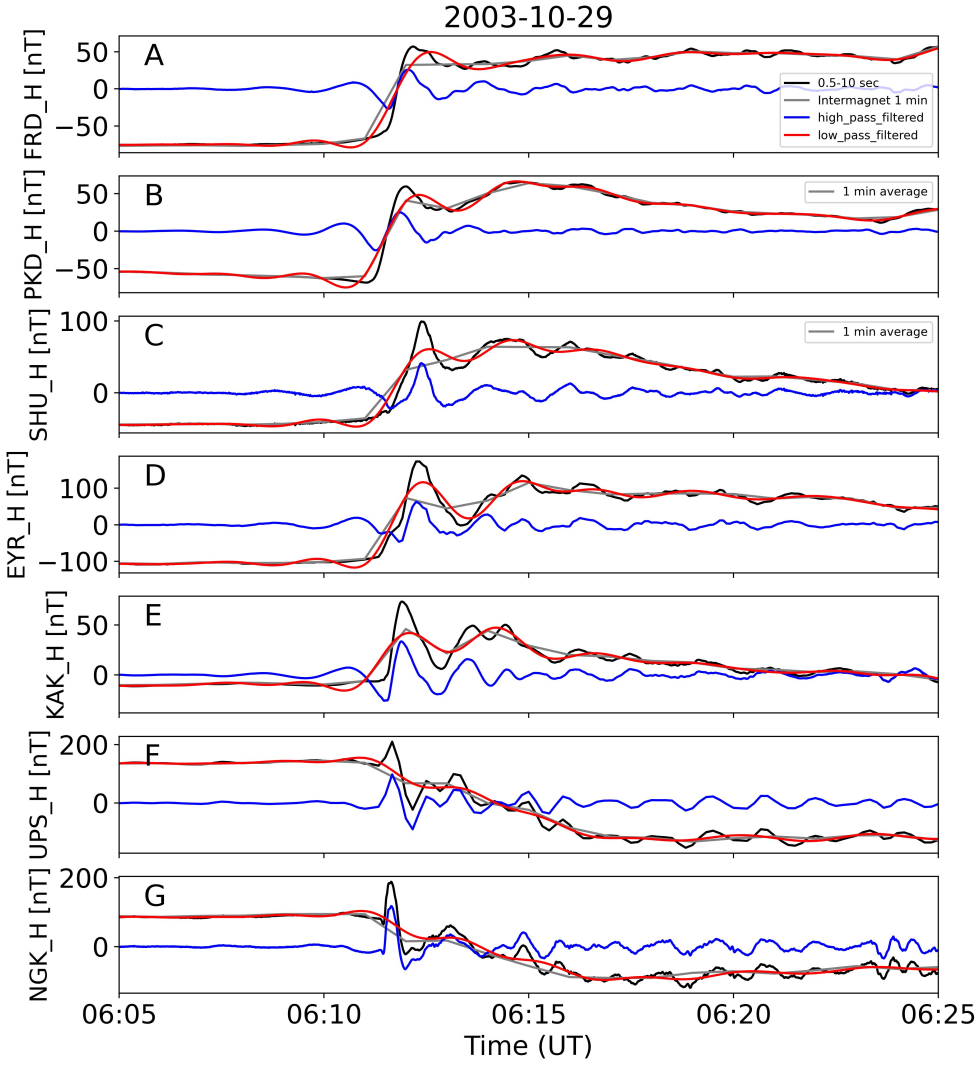

Figure 2. The horizontal magnitude of **B**, H, is shown at 7 locations indicated in Table 1; panel A is for FRD, B for PKD, C for SHU, D for EYR, E for KAK, F for UPS, and G for NGK. In all panels, black curves are for measurements sampled at 0.1-2 Hz (see Table 1 for specific sampling rate at each site), blue curves are for high-pass filtered measurements ($f > 0.0083$ Hz), and red curves are for low-pass filtered measurements ($f < 0.0083$ Hz). Light gray curves are for measurements sampled at 0.016 Hz obtained from either INTERMAGNET (all panels except B and C) or from a centered 60 s boxcar average (panels B and C).

tween the low- and high-pass filtered time series at each site rather than differences in amplitude between different sites, we use different y-axis ranges for each panel; see SI Figure S2 for data presented with the same y-axis range. Figure 2A and 2B show a step-like increase (SSC) starting just after 0611 UT in H (black curves) that is mostly captured in low-pass filtered measurements at FRD and PKD (red curves). There are smaller amplitude H variations with $f > f_{Nyquist60}$ (blue curves) that are not present in the 60 s samples (compare black and gray lines). Panel C is for a station (SHU) at a higher magnetic latitude and closer to local midnight. Here, wave activity is more evident in the original 1 s samples and high-pass filtered measurements; several wave cycles can be seen in the black and blue curves. Panels D and E for the EYR station in New Zealand and KAK station in Japan are similar to SHU, including a step-like increase along with H variations with $f >\sim f_{Nyquist60}$ (blue line) that are not captured in 60 s data from INTERMAGNET. Finally, panels F and G of Figure 2 are for the UPS (Sweden) and NGK (Germany) stations; the step-like increase is not visible, and H primarily has variations with $f > f_{Nyquist60}$. Note that the UPS and NGK stations bracket the locations where disruptions occurred in the Swedish power grid at 0611 and 0612 UT on 29 October 2003 (Pulkkinen et al., 2005), and the UPS site is at a similar magnetic latitude and longitude to a Finnish gas pipeline where GIC variations were observed with similar periodicities near this time (Viljanen et al., 2006, black curves in their Figure 6).

In Figure 3, we place these H measurements in context with Halloween storm measurements from later time periods at EYR, examining the entire storm as well as shorter intervals corresponding to periods with intense GIC at the nearby ISL site (section 2.4). Figure 3A and 3B show EYR H measurements over the three day period from 29-31 October 2003. Panel A shows measurements sampled at 0.2 Hz (black line) and the same data low-pass filtered (red line, $f < f_{Nyquist60}$), while Panel B shows high-pass filtered measurements (blue line, $f > f_{Nyquist60}$). The fact that the red and black lines lie almost on top of each other for much of the storm indicates that the overall H variation is dominated by variations with frequencies $f < f_{Nyquist60}$. However, variations with $f > f_{Nyquist60}$ have amplitudes of up to 50 nT during several portions of the storm (Panel B). The vertical dashed gray lines indicate two shorter intervals shown in Panels C and D; 0600-0700 UT on 29 October 2003 (an extended portion of the interval investigated in Figure 2) in Panel C, and 0200-0300 UT on 31 October 2003 in Panel D. ULF wave activity is seen in both panels. Note that maximum and minimum values differ across panels because different baseline values were removed (corresponding to the mean value for each time range) to make it easier to compare variations; the range of variation is the same in each panel. These shorter time intervals correspond to the storm periods with largest GIC amplitudes (described in section 2.4) and largest $f > f_{Nyquist60}$ wave amplitudes (blue curves in panel B), but not to the periods with the largest overall magnetic disturbance amplitude (panel A). Some of the $f > f_{Nyquist60}$ variations shown in Figure 3 are caused by disturbances with a broadband frequency spectrum rather than ULF waves. More generally, broadband disturbances such as the step-like increase in H caused by the SSC can occur at the same or nearly the same time as ULF waves and make significant contributions to H, $\mathbf{E}$, and GIC, making it difficult to quantify the relative contributions from ULF waves and other disturbances with frequency content above $f_{Nyquist60}$. We return to these points in section 3.

Figure 4 is for a widely used proxy for $|E|$, $\frac{dB_H}{dt}$, hereafter referred to as H'; this proxy for EYR $|E|$ has been shown to correlate well with nearby ISL GIC measurements (Rodger et al., 2017). Panel A is for H' measurements from EYR sampled at 5 s (black) and subsequently low-pass filtered (red, $f < f_{Nyquist60}$) during the 29-31 October 2003 storm interval. Panel B is for high-pass filtered 5 s H' measurements (blue, $f > f_{Nyquist60}$). Comparing panels A and B, much of the frequency content in H' is contained in $f > f_{Nyquist60}$, particularly during periods with the largest H'. This is seen, for example, by noting that the maximum and minimum values of the black line in panel A are often much larger than the corresponding values in the red line ($f < f_{Nyquist60}$). More direct, quan-

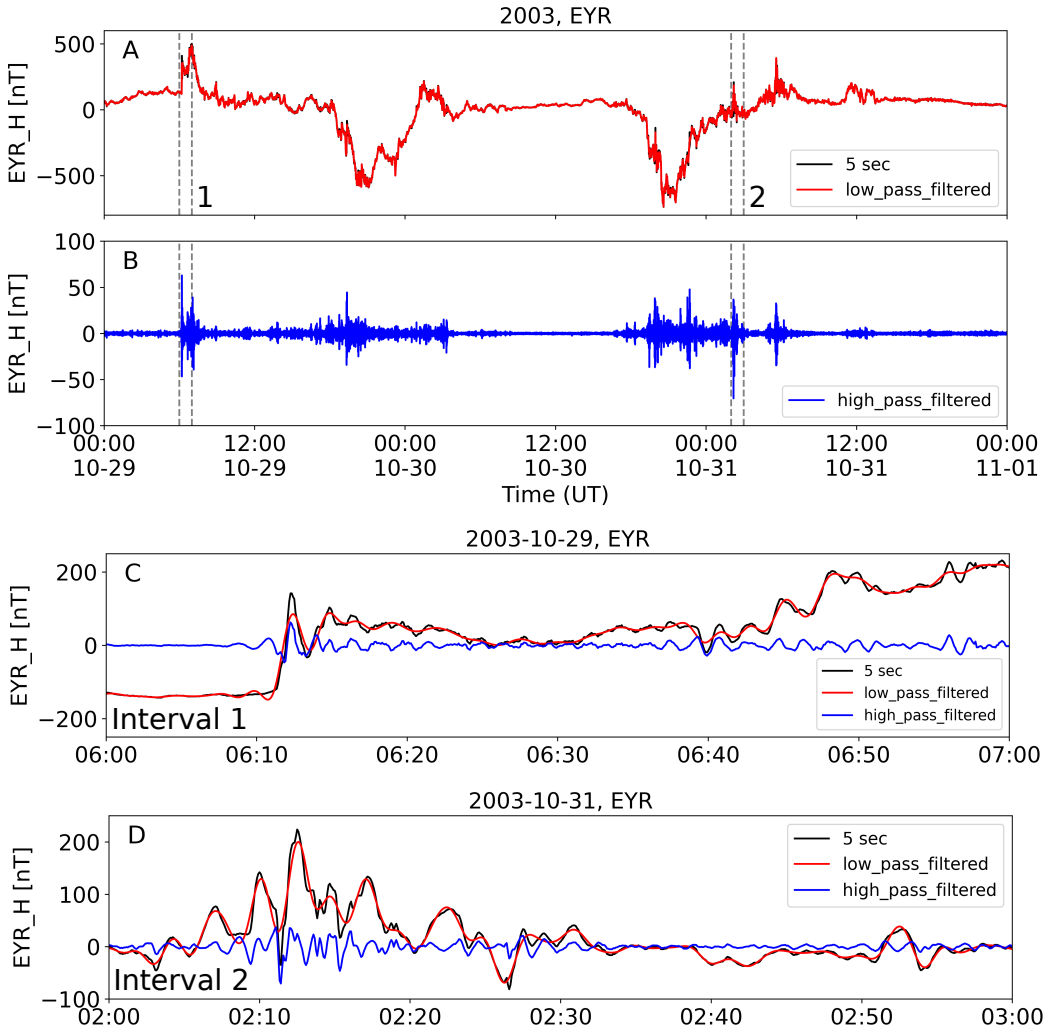

Figure 3. A) H measurements from EYR sampled at 5 s (black) and subsequently low-pass filtered (red, $f < f_{Nyquist60}$) for the 29-31 October 2003 storm interval. B) High-pass filtered EYR measurements ($f > f_{Nyquist60}$). C) 5 s (black), low-pass filtered (red), and high-pass filtered (blue) H observations at EYR on 29 October 2003 from 0600-0700 UT, the interval marked by vertical dashed lines on panels A and B. D) The same as C but for 31 October 2003 from 0200-0300 UT, with this interval also marked by vertical dashed lines in panels A and B.

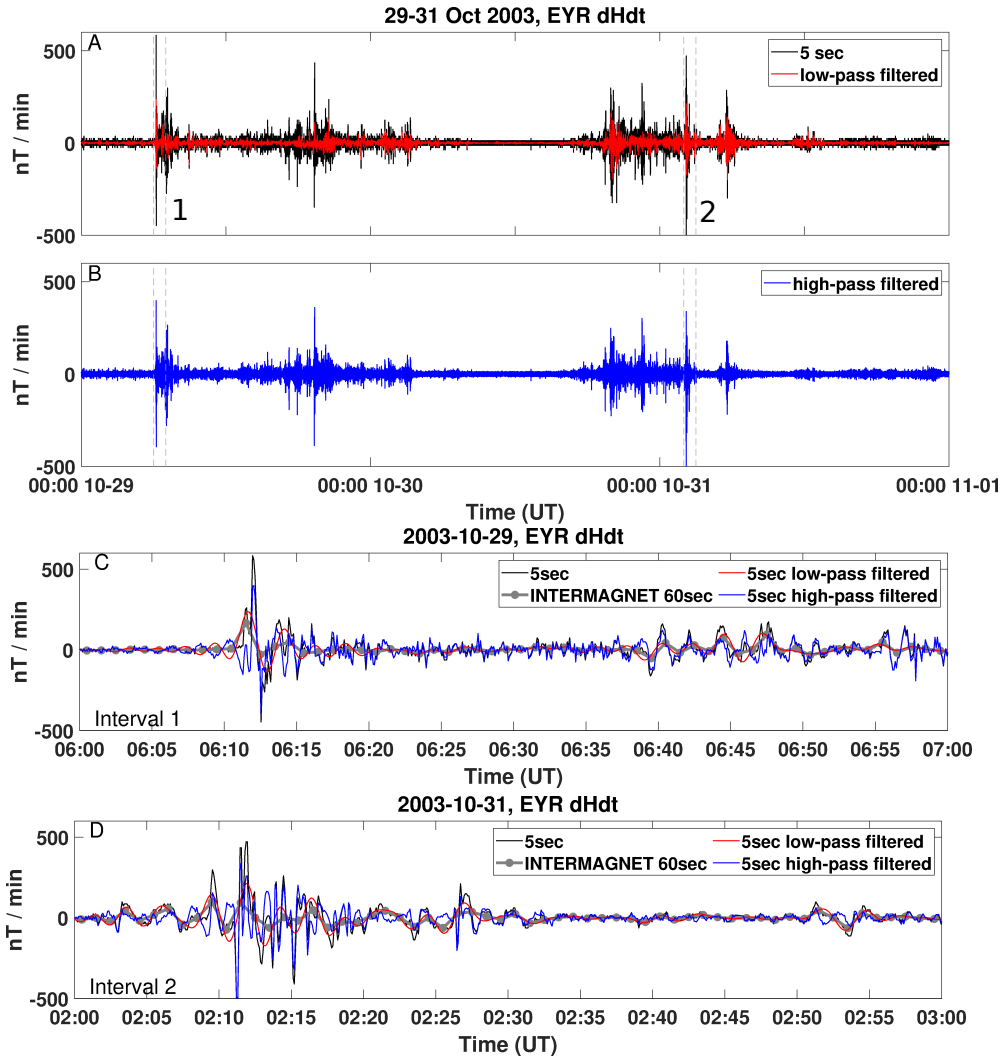

Figure 4. H' measurements from EYR sampled at 5 s (black) and subsequently low-pass filtered (red, $f < f_{Nyquist60}$) for the 29-31 October 2003 storm interval. B) High-pass filtered EYR H' measurements ($f > f_{Nyquist60}$). C) 5 s (black), low-pass filtered (red), and high-pass filtered (blue) H' observations at EYR on 29 October 2003 from 0600-0700 UT, the interval marked by vertical dashed lines on panels A and B. 60 s H' samples from INTERMAGNET are also shown for reference (gray lines). D) The same as C but for 31 October 2003 from 0200-0300 UT, with this interval also marked by vertical dashed lines in panels A and B.

Table 2. Maximum and Minimum Values of H' at EYR (nT/min), E_y at KAK (mV/km), and ISL M6 GIC (A) during the entire 29-31 October 2003 storm interval and shorter periods with ULF waves (Interval 1 on 29 October 2003 from 0600-0700 UT, Interval 2 on 31 October 2003 from 0200-0300 UT). 34.1 A and 583 nT/min correspond to the largest ISL M6 GIC and EYR H' measurements during the storm, and they are also 14-year peak values. Additional maximum and minimum values are shown in SI Tables S1 and S2.

Data Type	Max 29-31 Oct	Min 29-31 Oct	Max Int. 1	Min Int. 1	Max Int. 2	Min Int. 2
EYR H', nT/min 5 s	583	-521	583	-447	472	-521
EYR H', nT/min 1 s low-pass	236	-198	236	-138	212	-172
EYR H', nT/min 60 s INTERMAGNET	166	-171	166	-52	99.3	-73.5
KAK E_y, mV/km 1 s	398	-644	203	-644	268	-640
KAK E_y, mV/km 1 s low-pass	396	-490	126	-308	217	-437
KAK E_y, mV/km 60 s low-pass (second 00)	393	-476	111	-297	191	-350
ISL M6 GIC, A 4 s			34.1	-6.72	23.2	-17.7
ISL M6 GIC, A 4 s low-pass			20.4	-2.95	18.3	-8.1

titative evidence that much of the frequency content in H' is contained in $f > f_{Nyquist60}$ can be seen in power spectra and integrated power comparisons for $f < f_{Nyquist60}$ and $f > f_{Nyquist60}$ in SI Figures S3 and S4. For example, panel B of Figure S4 shows that the power contained in frequencies above $f_{Nyquist60}$ is greater than or equal to power from frequencies below the Nyquist frequency during much of the storm; the ratio of higher frequency power to lower frequency power is usually greater than 1.

Figure 4C and 4D are for the same time intervals as Figure 3C and 3D: 29 October 2003 0600-0700 UT and 31 October 2003 0200-0300 UT. In each panel, 5 s (black), low-pass filtered (red), and high-pass filtered (blue) H' observations are shown; a gray line corresponding to H' calculated with INTERMAGNET 60 s measurements is also shown for reference. In panel C, H' variations with $f > f_{Nyquist60}$ make up the largest contribution to the peak value of 583 nT/min at 0612 UT (note the correspondence between the blue and black lines at that time) and also have roughly equal contributions with variations having $f < f_{Nyquist60}$ during a sustained period with ±100 nT/min amplitude ULF wave activity with $f \sim f_{Nyquist60}$ starting well after the SSC at 0640 UT (compare red and blue lines from 0640-0700 UT). Panel D shows similar results for the second interval. Here, variations with a mix of frequencies are present (consistent with power spectra results shown in SI Figures S3 and S4), with sinusoidal H' variations with $f > f_{Nyquist60}$ evident from 0200-0230 UT producing maximum/minimum values in H' of roughly ± 500 nT/min. The largest contributions to H' during these two intervals are not present in the INTERMAGNET 0.016 Hz (1 min) data.

Table 2 summarizes maximum and minimum values for H' across the entire 3-day interval and for the two shorter intervals shown in Figures 3 and 4; recall that the two shorter intervals correspond to times with the largest ISL M6 GIC amplitudes. Across the entire storm, the maximum and minimum values of H' are 583 and -521 nT/min for the 5 s sampling interval, 236 and -198 nT/min for low-pass filtered 5 s data, and 166 and -171 nT/min for INTERMAGNET 60 s data. Substantial differences are also found in the two shorter intervals. For example, during Interval 2 on 31 October 2003 from 0200-0300 UT, H' has a range of 993 nT/min in the original 5 s measurements and 173 nT/min in the 60 s INTERMAGNET measurements. Further results for H' are listed in SI Table S1, including a comparison of values when using different resampling methods. Table 2 of Rodger et al. (2017) showed that the maximum H' recorded in the 5 s EYR data during geomagnetically disturbed periods between 2001-2015 was 583 nT/min; this occurred on 29 October 2003 at 0611 UT, the same period shown in Figure 2. Thus, the H' measurements examined in Figures 2-4 have values equal or comparable to the maximum H' recorded at EYR during geomagnetically disturbed periods across that 14-year interval.

2.3 Geoelectric Field Measurements

We next review **E** measurements at a few of the locations discussed in Table 1 with available data. Figure 5A and 5B are for the x and y component (x is for geographic north and y is for geographic east) of **E** at the PKD station in the United States. As before, the black curves are for the original **E** measurement sampled at 1.0 Hz, and red and blue curves are for low-pass and high-pass filtered 1.0 Hz measurements (cutoff frequency at $f_{Nyquist60}$). Figure 5C and 5D are for **E** measurements at the NGK station in Germany; the primary contributor to NGK **E** variations is from $f > f_{Nyquist60}$ (variations in the black curves mostly match the blue curves). Figure 5E and 5F are for KAK **E** measurements in Japan. At both KAK and NGK, the wave amplitudes in the high-pass filtered measurements often exceed the wave amplitudes in the low-pass filtered measurements (compare red and blue curves in the bottom four panels).

Figure 6 is for the geographic y component of **E** at KAK for the entire three day-interval, presented in a similar format as Figures 3 and 4 for EYR magnetic field measurements (the x component of **E** at KAK is show in SI Figure 5). Panel A is for 1 s (black) and subsequently low-pass filtered (red, $f < f_{Nyquist60}$) measurements, while panel B is for high-pass filtered (blue, $f > f_{Nyquist60}$) measurements. The low- and high-pass filtered time series have comparable amplitudes during many portions of the storm (compare red curve in panel A to blue curve in panel B), particularly during the periods with the largest E_y amplitudes. This is also consistent with dynamic power spectra and integrated power shown in SI Figure 4; for example, SI Figure 4D shows that while integrated power at $f > f_{Nyquist60}$ is usually smaller than integrated power at $f < f_{Nyquist60}$ during the entire 3-day interval, the ratio of the two quantities is usually close to 1 at times when the power (E_y amplitude) is largest. Figure 6C and D for the shorter time intervals on 29 October 2003 from 0600-0700 UT and 31 October 2003 from 0200-0300 UT also show this. Panel C shows that the higher frequencies continue to make significant contributions to the overall E_y variations well after the SSC (note the comparable amplitudes of red and blue curves). Panel D shows that in the later period, lower frequencies have larger amplitudes, but the higher frequencies have amplitudes within a factor of two or three.

The maximum value of E_y of 0.644 V/km at KAK shown in Figure 5 (black line, see also SI Table S2 for $|\mathbf{E}|$ which is 0.658 V/km) is the largest value measured at that location during the 3-day interval from 29-31 October 2003 when considering measurements sampled at 1.0 Hz. Unfortunately, there are no long-term statistics available for the 1 s **E** measurements at KAK to benchmark this value, but we can compare with long-term statistics based on longer sampling intervals:

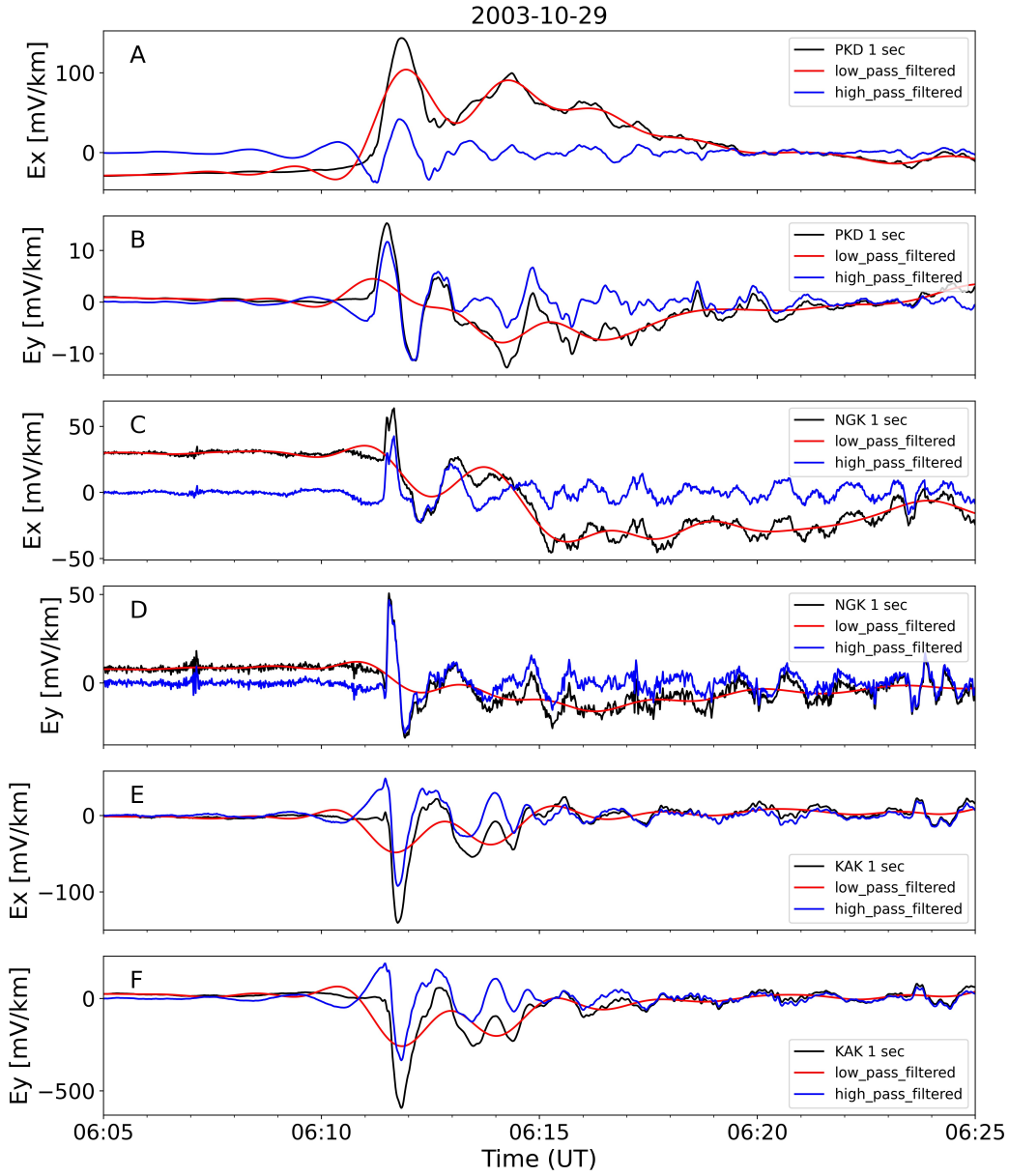

Figure 5. Geoelectric field measurements from PKD (United States, Panels A and B), NGK (Germany, Panels C and D), and KAK (Japan, Panels E and F). Panel A is is for the geographic x component of **E** measured at the PKD site with black lines for the data sampled every 1 s, red-lines for low-pass filtered 1 s data ($f < f_{Nyquist60}$ as in other Figures), and blue lines for high-pass filtered 1 s data ($f > f_{Nyquist60}$). Panel B is similar to A, but for the y component of **E**. Panels C/D and Panels E/F are in the same format as Panels A/B, but for NGK and KAK, respectively.

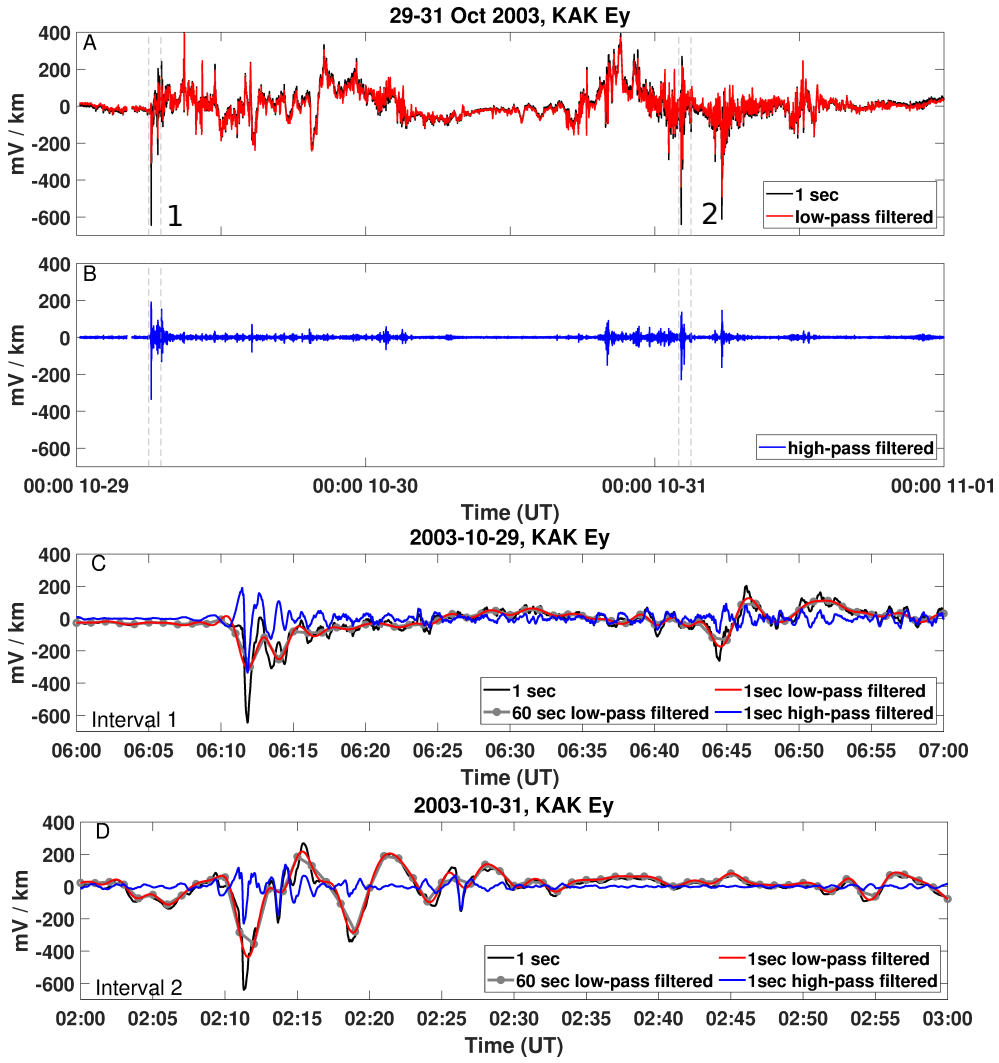

Figure 6. A) The geographic y component of geoelectric field measurements at KAK sampled at 1 s (black) and subsequently low-pass filtered (red, $f < f_{Nyquist60}$) for the 29-31 October 2003 storm interval. B) High-pass filtered E_y measurements ($f > f_{Nyquist60}$). C) 1 s (black), low-pass filtered (red), low-pass filtered and resampled to 60 s intervals centered at second 00 of the minute (gray dotted), and high-pass filtered (blue) E_y observations on 29 October 2003 from 0600-0700 UT, the interval marked by vertical dashed lines on panels A and B. D) The same as C but for 31 October 2003 from 0200-0300 UT, with this interval also marked by vertical dashed lines in panels A and B.

1. Fujii et al. (2015) considered **E** measurements with 3600 s (one hour) sampling interval during an 11-year monitoring interval from 1 January 2000 to 28 February 2011 (see their Figure 2), finding maximum **E** variation amplitudes more than a factor of two lower than 0.644 V/km.
2. Zhang and Ebihara (2022) used 60 s **E** measurements from KAK to perform superposed epoch analysis of **E** during different types of driving conditions, including SSC. They estimated a 100-year extreme value for SSC-related horizontal **E** magnitude of 0.612 V/km at KAK when using 60 s data (Table 2 of Zhang and Ebihara (2022)); this value was exceeded in the 29 October 2003 storm when considering 1 s data (Figure 5, SI Table S2 of this study, 0.658 V/km).

As shown in these examples and Table 2 and SI Table S2, the 1 s data can produce roughly a factor of two or larger peak values of **E** when compared to 3600 s (one hour) and 60 s (one minute) data. The smaller peak values in 3600 s and 60 s data are due in part to the undersampling or removal of ULF waves with $f > f_{Nyquist60}$ expected at KAK's magnetic latitude (Figure 1). The SSC observed at KAK on 29 October 2003 was large but not the largest ever recorded (e.g., Araki et al., 1997); thus it is somewhat surprising that the 100-year peak value of SSC-related **E** predicted by Zhang and Ebihara (2022) (when using 60 s data) was realized for the 29 October 2003 SSC (when using 1 s data). This result is at least partly related to ULF waves that are concurrent with SSC (Saito & Matsushita, 1967; Araki et al., 1997) being (1) undersampled in 60 s measurements and (2) averaged out during superposed epoch analysis due to wave phase/frequency varying from event to event.

2.4 Geomagnetically Induced Current Measurements

We next examine ISL M6 GIC measurements from New Zealand (located very close to EYR [Table 1]). Figure 7A shows H' sampled at 0.2 Hz at EYR and is provided for reference to compare against GIC measurements. Figure 7B is for ISL M6 GIC measured throughout the 29-31 October 2003 storm. The largest amplitude GIC tends to occur at the same time as large values of H' at EYR, consistent with the finding from Rodger et al. (2017) that these two measurements are well-correlated. Figure 7C shows GIC measurements during the 29 October 2003 SSC. As in Figure 6, the black line is for the 4 s measurements; the red for low-pass filtered measurements ($f < f_{Nyquist60}$); the gray dotted line for low-pass filtered measurements resampled to 60 s centered at second 00 of the minute; and the blue for high-pass filtered measurements ($f > f_{Nyquist60}$). The largest GIC magnitude of 34.1 A during a 14-year monitoring interval (Table 1 in Rodger et al., 2017) corresponds to the period with the spike and subsequent variations in H' seen in panel A. Starting from that initial increase, GIC variations with $f \sim f_{Nyquist60}$ continue with decaying intensity until approximately 0640 UT, when they begin increasing in intensity again with amplitudes of ∼10 A. This trend of decaying then increasing variation amplitude is also seen in H' (Figure 4C, see also Figure S6). For much of the interval, frequencies above and below $f_{Nyquist60}$ have comparable GIC amplitudes, as evidenced by the comparable amplitudes of the red and blue curves. Table 2 further compares maximum and minimum GIC values before and after low-pass filtering during this interval. In the original measurements, the maximum and minimum values are 34.1 A and -6.72 A, whereas for $f < f_{Nyquist60}$ they are 20.4 A and -2.95 A. The range of GIC variation (i.e., maximum value in the one hour interval minus the minimum value, see Table 2) is a factor of 1.74 larger in the original measurements (40.8 A compared to 23.4 A), further indicating that the GIC has significant frequency content above $f_{Nyquist60}$.

Panel D of Figure 7 is for the later period from 0200-0300 UT on 31 October 2003. GIC variations with $f >\sim f_{Nyquist60}$ are seen throughout this interval with growing and then decaying amplitudes. Note that panels C and D both have a y-axis range of 45 A. Although the peak GIC is larger in the first event (34.1 A, panel C), the range of GIC values is similar in both events, including the rapid change from -17.7 to +23.2 A

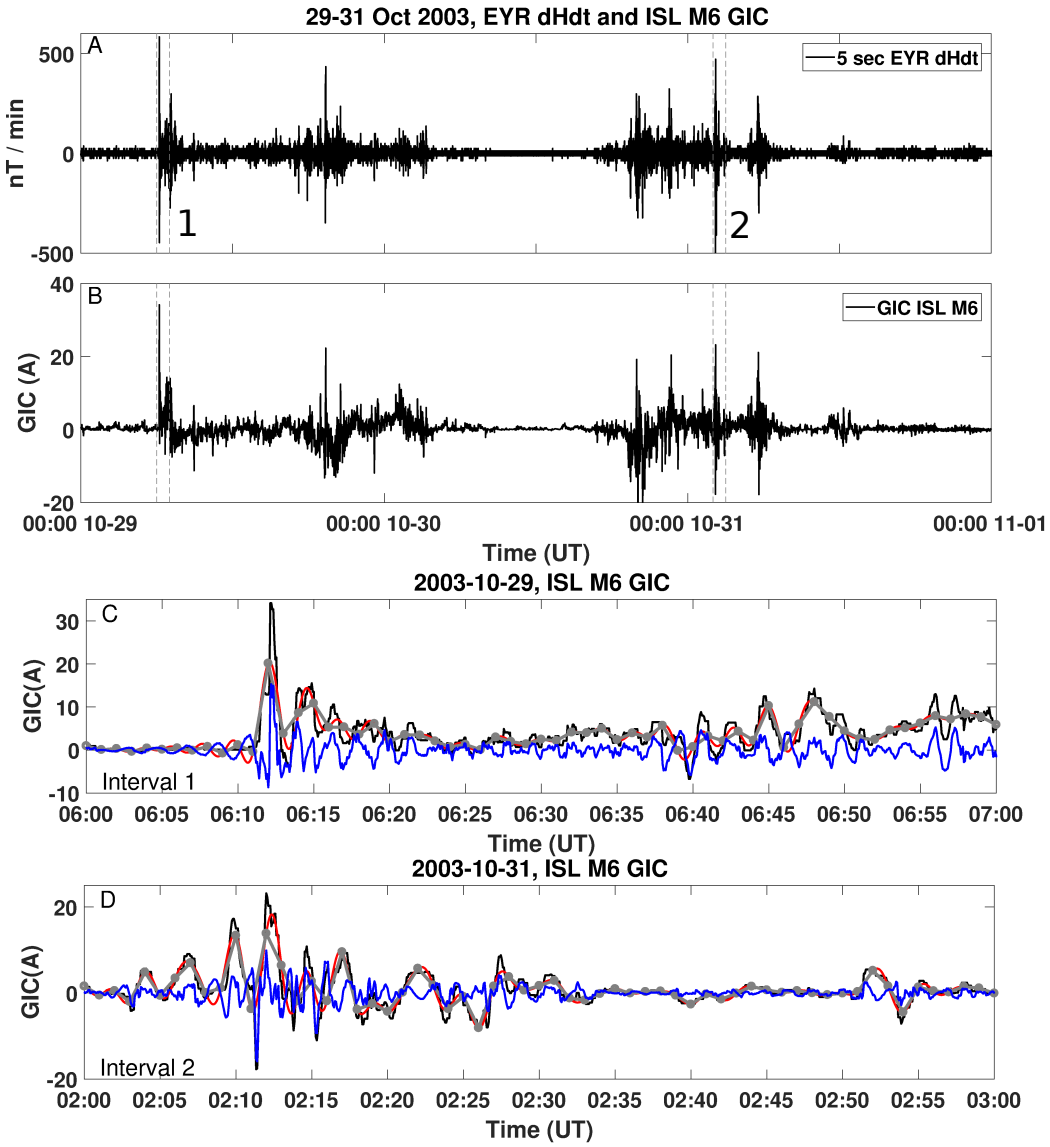

Figure 7. H' and GIC measured in New Zealand (EYR and ISL M6). A) H' sampled at 0.2 Hz. B) ISL M6 GIC measurements with variable sampling rate (see section 2.1) but usually 0.25 Hz during the periods of interest marked by vertical dashed gray lines. C) ISL M6 GIC measurements on 29 October 2003 0600-0700 UT, interpolated to a uniform sampling interval of 4 s (the original data are nearly identical since the sampling interval is 4 s for most of the interval) in the black line, low-pass filtered ($f < f_{Nyquist60}$, red) 4 s GIC measurements, low-pass filtered GIC measurements resampled to 60 s intervals centered at second 00 of the minute (gray dotted), and high-pass filtered 4 s GIC measurements ($f < f_{Nyquist60}$, blue). D) Same as C but for the time interval 31 October 2003 0200-0300 UT.

(40.9 A range, panel D). Similar to H' and E_y results in Figure 4 and SI Figures S3 and S4, there are multiple frequencies present in the GIC measurements shown in Figure 7D (variations are present in both the red and blue curves); those with $f >\sim f_{Nyquist60}$ make significant contributions throughout the interval, including a large negative GIC that is not captured in the low-pass filtered measurements. The GIC correlate best with the 5 s H' in Figure 4C,D (black curves) rather than the 60 s H' from INTERMAGNET (gray curves) or the low-pass filtered 5 s H' measurement. The bottom two rows of Table 2 further compare maximum and minimum GIC values before and after low-pass filtering during this interval. In the original measurements, the maximum and minimum values are 23.2A and -17.7 A, whereas for $f < f_{Nyquist60}$ they are 18.3 and -8.1 A. The range of GIC variation is a factor of 1.55 larger in the original measurements, (40.9 A compared to 26.4 A), again indicating that the GIC has significant frequency content above $f_{Nyquist60}$.

Rodger et al. (2017) reported statistical results pertaining to ISL M6 GIC measurements from 2001 to 2015. Their Table 2 shows that the maximum GIC at this location occurred during the 29 October 2003 SSC at 0611 UT (34.1 A, interval shown in Figure 4C of this study). All entries in their Table 2 correspond to periods when the EYR 60 s H' exceeds 40 nT/min, and the range of GIC intensities for the other 30 events in their list is 4.6-33.1 A. Thus, to the extent that any source of ISL M6 GIC during the 14-year monitoring interval could be regarded as significant (i.e., produce large amplitude GIC), the waves with frequencies $>\sim f_{Nyquist60}$ are significant. They can generate GIC variation amplitudes of roughly 10-20 A (blue line in panel D of Figure 7), comparable to the maximum value of 34.1 A over the 14-year monitoring interval. They also likely contribute to the peak value of 34.1 A itself, as they may occur at the same time as the magnetopause current intensification that gives rise to the step-like increase in **B** during the SSC (interval 1 in Figure 3, see further discussion in section 3). These waves can also be regarded as potentially hazardous, as these GIC intensities are comparable to the ISL M6 measurement of 33.1 A when a transformer failure occurred farther south in Dunedin/Halfway Bush, New Zealand, on 6 November 2001 (Marshall et al., 2012). No GIC measurements were available at the location of the transformer that failed, but it was roughly estimated to experience a 100 A magnitude GIC (Rodger et al., 2017). When examining time series over a 27-hour period during the 29-31 October 2003 storm, Rodger et al. (2017) noted that the **B** measurements sampled at 0.2 Hz, "have a more similar time variation to that seen in the GIC measurement...suggesting that the higher time resolution magnetic field measurements are better at capturing the driving of the GIC." As we have shown in Figure 7, this is due at least in part to the removal of ULF wave activity in 60 s measurements. Although 60 s **B** (H') measurements didn't match the time variation of the ISL M6 GIC measurements during many periods of peak GIC for the 29-31 October 2003 storm, there were other periods of the storm with elevated GIC where they matched well. In general, the suitability of H' (which tends to overweight higher frequencies, Heyns et al., 2021) as a proxy for **E** and the correlation of H' with GIC will vary by location and event depending on local ground conductivity, the frequency content of H in a given event, and the power system of interest.

3 Discussion

In this section, we return to the question from Trichtchenko (2021), "What should be the sampling rate (or Nyquist frequency) in order to provide an adequate representation of...pulsations...for use in the calculations of the extreme geoelectric field values and in the GIC modeling?" Recall from section 1 that results from previous studies suggested that the largest amplitude ULF-wave driven **B** and GIC would occur in the 120-600 s (2-10 minute) period range, thus a 60 s sampling interval would be appropriate for extreme value analysis and GIC modeling related to ULF waves. These results were based in large part on **B** and GIC measurements from magnetic latitudes >∼60 degrees.

As this study shows, the situation is different at magnetic latitudes < 60 degrees for two reasons: (1) past theory, modeling, and observational work show that most ULF wave modes have $f >\sim f_{Nyquist60}$ (section 1, Figure 1) and (2) the observations shown in section 2 indicate waves with $f >\sim f_{Nyquist60}$ are associated with H', **E**, and GIC amplitudes comparable to the largest values recorded during extended monitoring intervals in Japan and New Zealand. Thus, we argue that the appropriate range for sampling ULF waves at magnetic latitudes below 60 degrees is 0.1-1.0 Hz (sampling interval 1-10 s), with the particular sampling rate depending on the magnetic latitude range of interest due to the magnetic latitude dependence of standing Alfvén wave frequency (section 1). This frequency range applies to all storm phases since these waves can occur at any time and are not limited to, for example, SSC's or storm main phase. Considering the example of the 29-31 October 2003 storm, the results shown in section 2 indicate a sampling rate of 0.1 Hz would have worked well at most locations, even the low latitude KAK station, during periods when the largest **E** and GIC were observed; however, there were some intervals at EYR with significant power at 0.1 Hz, suggesting that a sampling rate of at least 0.2 Hz was needed (Figure 7 and SI Figures S3 and S4). During the 24 March 1991 geomagnetic storm, SSC high frequency waves that drove intense H' and **E** likely would have required a 1.0 Hz sampling rate, as noted by Araki et al. (1997) and Kappenman (2003).

The H variations shown in Figures 2-4 are associated with a variety of magnetosphere-ionosphere current systems and waves. The transient, step-like increase in H seen at multiple locations at 0611 UT on 29 October 2003 was caused by the intensification of magnetopause currents and a magnetosonic wave, both triggered in response to a solar wind dynamic pressure increase; together they generate the step-like ground magnetic disturbance seen at low latitudes (Araki, 1994). There are also several types of ULF waves present in these figures. As seen in Figure 1, the frequencies of the ULF wave activity seen in the blue curves in Figures 2-4 are consistent with standing Alfvén waves and plasmaspheric cavity modes/virtual resonances, whereas the wave activity seen in the red curves may also include global cavity/waveguide modes reported in past studies (e.g., Marin et al., 2014). These current systems and waves can occur simultaneously. For example, the magnetosonic wave triggered by the solar wind pressure increase can itself trigger (i.e., form the first wave cycle of) a standing magnetosonic wave if sufficient wave energy is reflected in the magnetospheric cavity (e.g., Yu & Ridley, 2011; Takahashi et al., 2018), and standing magnetosonic waves and standing Alfvén waves can occur simultaneously and with multiple harmonics as discussed in section 1. ULF waves are commonly observed in conjunction with SSC, similar to the 29 October 2003 SSC (Saito & Matsushita, 1967; Wedeken et al., 1986; Araki et al., 1997).

When selecting an appropriate sampling rate for ULF waves for GIC studies, there are other important factors to consider besides the magnetic latitude:

1. The conducting structure of the Earth: As shown in Bedrosian and Love (2015), even a spatially uniform, sinusoidal **B** results in a non-uniform **E** with regional variations in polarization and intensity that depend on the frequency of **B**. Different regions may respond more (or less) to higher frequency geomagnetic variations (Grawe et al., 2018).
2. The properties of the power system of interest: Recent modeling and observational work suggests that sinusoidal **E** oscillations may couple to GIC in different ways when compared to more impulsive or irregular variations with longer periods. The coupling is frequency dependent, and the coupling at different frequencies depends on the properties of the power system/network such as the network orientation and reactive power response of transformers in the network (Oyedokun et al., 2020; Heyns et al., 2021; Heyns et al., 2020). When considering the impact of GIC on a power system, it is also clearly important to allow for factors that control GIC-

produced half-cycle saturation, leading to the production of even order harmonic distortion (e.g., Clilverd et al., 2018; Rodger et al., 2020; Clilverd et al., 2020).

3. The choice of filter: To reduce aliasing of higher frequency signals, many 60 s measurements provided via INTERMAGNET use an anti-aliasing filter that attenuates signals close to $f_{Nyquist60}$, leading to differences in maximum values of H' when a digital filter with a relatively flat frequency response near $f_{Nyquist60}$ is used (Table 2, SI Table S1, compare INTERMAGNET values to resampled low-pass filtered values). As shown in Figures 6 and 7 (compare red and gray curves in panels C and D) and SI Table 2, even when a filter with a relatively flat response is used, resampling the filtered data to 60 s can lead to differences in maximum/minimum values depending on the sampling convention (centered at second 00 of minute, second 30 of minute, etc.) due to the short duration that the maximum/minimum values occur. In general, the filter properties should be carefully considered in conjunction with the sampling rate when estimating extreme values of **B**, H', **E**, and GIC related to ULF waves with $f \sim f_{Nyquist}$ (Figure 1).

As discussed in section 1 and shown in sections 2.2, 2.3, and 2.4, ULF waves with $f > f_{Nyquist60s}$ are not captured in measurements with sampling intervals of 60 s, whereas lower frequency variations and impulses/step-like variations with a broadband frequency spectrum are fully or at least partially captured in these data. When these higher frequency waves are present, event-specific conclusions concerning the magnetosphere-ionosphere current systems that drive **B**, **E**, and GIC may differ significantly when examining measurements collected with different sampling intervals. Figure 8 illustrates these points further. Three different situations are shown where the magnetopause current intensification related to a solar wind pressure pulse dominates H (panels A and D); a ULF wave dominates (panels B and E); and both are present with roughly equal peak intensities (panels C and F). Panels A, B, and C show time series of H sampled at 1.0 Hz, while panels D, E, and F show the same data after application of a 60 s boxcar average and resampling to 60 s intervals. The situations in panels A, B, and C are qualitatively similar to the observations at FRD (step-like increase most intense), UPS/NGK (wave-like variations with $f > f_{Nyquist60}$ most intense), and EYR/KAK (both present), respectively, during the 29 October 2003 SSC (Figures 2 and 3). The time series shown in panels D, E, and F indicate that the contributions of the waves are removed when using 60 s data; in contrast, variations related to the step-like increase in magnetic field caused by the intensification of magnetopause currents are mostly preserved as they have a broadband frequency spectrum. If 60 s **B** measurements are subsequently used for calculations of **E** and predictions for GIC, the contributions of the waves with $f > f_{Nyquist60}$ to **E** and GIC would not be included.

These results have implications for choosing appropriate models of the underlying magnetosphere-ionosphere phenomena that drive the **E** and hence GIC. For example, while several studies have used self-consistent global magnetohydrodynamic simulation codes to study **B** related to magnetopause current intensifications and transient high-latitude field-aligned current systems (e.g., Fujita et al., 2003; Yu & Ridley, 2011; Ozturk et al., 2017), these same simulation codes are not always well-suited to examining ULF waves. There are several reasons for this, including over-damping due to the grid resolution being insufficient (e.g., Claudepierre et al., 2009; Hartinger et al., 2014, 2015), lack of appropriate boundary conditions such as plasmaspheric density (e.g., Claudepierre et al., 2016), and time steps that are too long to capture wave activity and transients with $f > f_{Nyquist60}$ (Shi, Lin, et al., 2022), all of which significantly impact the ability to model the frequency and amplitude of ULF waves that occur at magnetic latitudes below 60 degrees. When examining 60 s time series similar to the results in Figures 2-8, one may conclude that global MHD simulations with coarse spatial grid resolution and 60 s time steps would be sufficient to model the **B** during, e.g., the SSC, whereas examination of 0.1-1.0 Hz measurements would indicate that higher grid resolutions, shorter

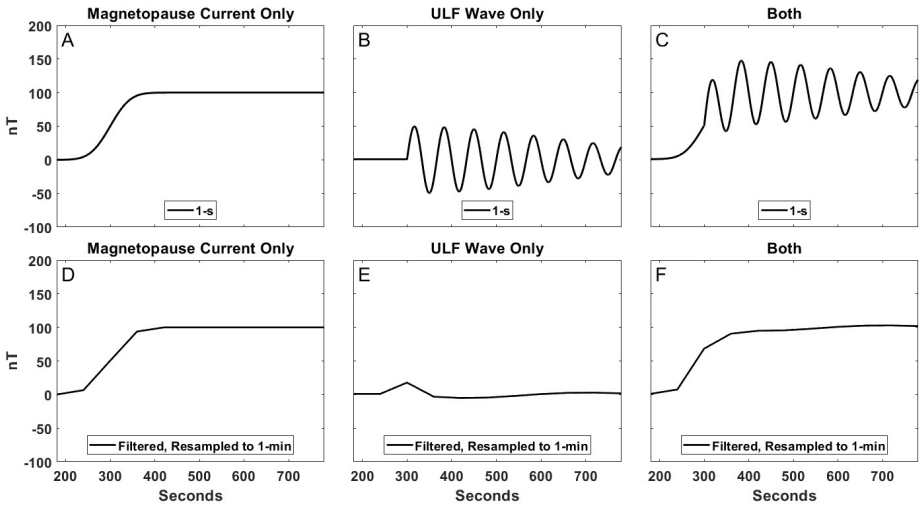

Figure 8. A) An example low latitude magnetic response to a solar wind pressure pulse-related magnetopause current intensification sampled at 1.0 Hz (solid black line). B) An example ULF wave generated by a pressure pulse sampled at 1.0 Hz. C) A superposition of the signals seen in A and B. D-F) The same signals as A-C, but after the application of a 60 s boxcar average.

time steps, and constraints on plasmaspheric mass density are needed to capture the wave activity.

As discussed in section 1, estimates for extreme **B**, **E**, and GIC increase when higher sampling rates are used, though the amount of the increase depends on location. We cannot say how large a contribution ULF waves with $f >\sim f_{Nyquist60}$ make to previously reported differences, though the results presented in this study suggest this is an important question that should be tested with further measurements sampled at 0.1-1.0 Hz collected during major geomagnetic storms, supplemented by numerical simulations of extreme events. For example, as noted in section 2.2, large amplitude waves with frequencies $>\sim f_{Nyquist60}$ were observed following SSC in southern Sweden in the Halloween storm; other SSC events with very similar wave activity have occurred and should also be investigated to determine when and where these waves represent a hazard (Wedeken et al., 1986). Rosenqvist et al. (2022) recently simulated an extreme SSC event in this region, finding that waves with similar or higher frequencies led to modeled GIC of roughly ±50-100 A (Figure 8 in that study). Similar simulations are needed for other extreme driving conditions and other regions to better estimate wave amplitudes during extreme events, given the limited availability of 0.1-1.0 Hz data during past time intervals with major geomagnetic storms.

4 Summary

In this study, we examined measurements during the 29-31 October 2003 storm and past ULF wave theory, modeling, and observational work to show (1) the appropriate sampling rate for capturing **B**, **E**, and GIC variations related to ULF waves is 0.1-1.0 Hz, with the specific value in that range dependent on magnetic latitude and (2) waves with frequencies $>\sim f_{Nyquist60}$ can drive significant and potentially hazardous GIC at magnetic latitudes below 60 degrees:

1. Theory, modeling, and observation work all indicate that many ULF wave modes (plasmaspheric fast mode resonances, standing Alfvén waves) occurring at magnetic latitudes below 60 degrees have $f > f_{Nyquist60}$ (section 1, Figure 1).
2. In this study, ULF wave variations in **B**, **E**, and GIC measurements with $f >\sim f_{Nyquist60}$ are present during several portions of the 29-31 October 2003 geomagnetic storm. These waves are undersampled in 60 s time series, leading to underestimates in maximum/minimum values of H', **E**, and GIC variations by roughly a factor of two or more when using 60 s data (Table 2). For example, during a period of ULF wave activity on 31 October 2003 0200-0300 UT, the range of EYR H' was 993 nT/min and 173 nT/min in 5 s and 60 s (INTERMAGNET) measurements, respectively.
3. ULF waves drive or contribute significantly to ISL M6 GIC variations in New Zealand with amplitudes comparable to the maximum value of 34.1 A occurring during a 14-year monitoring interval and to values related to a transformer failure. These waves also likely contribute to the peak value of 34.1 A itself, which occurred during the 29 October 2003 SSC. Thus, ULF waves with frequencies $>\sim f_{Nyquist60}$ are associated with significant and potentially hazardous GIC.

These results differ from past reports of **B** and GIC from magnetic latitudes > 60 degrees, where 2-10 minute wave periods ($f_{Nyquist60} > f > 0.0017$ mHz) were associated with the largest amplitude ULF wave **B** and GIC. At magnetic latitudes <60 degrees, waves with periods $<\sim$ 2 minutes can drive or contribute significantly to some of the largest **E** and GIC, for example, the largest GIC reported during a 14-year monitoring interval in New Zealand. A significant part of the world's population and industry fall in the geographic region where these shorter period waves occur.

The use of 60 s data misses contributions from ULF waves that occur at magnetic latitudes <60 degrees (Figure 1) since these waves have their frequency content concentrated above $f_{Nyquist60}$. In contrast, **B** and **E** variations at lower frequencies or with a broadband frequency spectrum are fully or partially retained in 60 s data. The absence of these waves in 60 s data can prevent the identification of these waves as a cause of extreme GIC and thus affect the choice of appropriate methods for modeling the GIC. It is likely these waves affect extreme value estimates in at least some locations (e.g., discussion in section 2.3).

Our results indicate that measurements sampled at 0.1-1.0 Hz and numerical simulations are needed to determine extreme values of **B** and **E** that may be associated with these waves. In the future, **B**, **E**, and GIC measurements consistently recorded at 0.1-1.0 Hz are needed at more locations to determine when, where, and how often these waves may represent a hazard to power systems at different magnetic latitudes, with different power system configurations, and with different local ground conductivities. Such data can be used, for example, to tailor global MHD simulation configurations used for space weather forecasts (Pulkkinen et al., 2021) to include contributions from ULF waves.

Open Research Section

The geomagnetic (quasi-dipole) latitudes provided were obtained using the IGRF model and calculator available from the British Geological Survey (`http://www.geomag.bgs.ac.uk/data\_service/models\_compass/coord\_calc.html`). The filtering software were obtained from the publicly available Python SciPy signal module (`https://docs.scipy.org/doc/scipy/reference/signal.html#module-scipy.signal`). The 60 s ground-based magnetic field data from FRD, EYR, KAK, UPS, and NGK are available from the INTERMAGNET repository (`https://www.intermagnet.org`). The PKD data are publicly available at the Northern California Earthquake Data Center hosted at the Berkeley Seismology Lab (`https://seismo.berkeley.edu/bdsn/em.overview.html`). The KAK data are publicly available at the Kakioka Magnetic Observatory (`https://`

www.kakioka-jma.go.jp/en/index.html). The USGS data are publicly available via Rigler and USGS Geomagnetism Program (2023) at https://doi.org/10.5066/P91S9DIF. The NGK and EYR data are available via Zenodo from Hartinger et al. (2022) at https://doi.org/10.5281/zenodo.7261515. We thank the institutes who maintain the IMAGE Magnetometer Array, including the Geological Survey of Sweden who maintains the UPS site; 10 s magnetometer data from UPS are available from IMAGE (https://space.fmi.fi/image/www/index.php?). The New Zealand LEM DC data were provided by Transpower New Zealand with caveats and restrictions. This includes requirements of permission before all publications and presentations. In addition, we are unable to directly provide the New Zealand LEM DC data or the derived GIC observations. Requests for access to the measurements need to be made to Transpower New Zealand. At this time the contact point is Michael Dalzell (michael.dalzell@transpower.co.nz). We are very grateful for the substantial data access they have provided, noting this can be a challenge in the space weather field (Hapgood et al., 2016).

Acknowledgments

M.D.H. and X.S. were supported by NASA 80NSSC19K0907. C.J.R., D.H.M., and T.P. were supported by New Zealand Ministry of Business, Innovation and Employment Endeavour Fund Research Programme contract UOOX2002. We thank Dr. Anna Kelbert for discussions and insight related to magnetotelluric transfer functions. Any use of trade, firm, or product names is for descriptive purposes only and does not imply endorsement by the U.S. Government.

References

Apatenkov, S. V., Pilipenko, V. A., Gordeev, E. I., Viljanen, A., Juusola, L., Belakhovsky, V. B., ... Selivanov, V. N. (2020). Auroral Omega Bands are a Significant Cause of Large Geomagnetically Induced Currents. *Geophysical Research Letters*, *47*(6), e86677. doi: 10.1029/2019GL086677

Araki, T. (1994). A physical model of the geomagnetic sudden commencement. In M. Engebretson, K. Takahashi, & M. Scholer (Eds.), *Solar wind sources of magnetospheric ultra low frequency waves* (p. 183-200). American Geophysical Union (AGU). doi: https://doi.org/10.1029/GM081p0183

Araki, T., Fujitani, S., Emoto, M., Yumoto, K., Shiokawa, K., Ichinose, T., ... Liu, C. F. (1997). Anomalous sudden commencement on March 24, 1991. *Journal of Geophysical Research: Space Physics*, *102*(A7), 14075-14086. doi: 10.1029/96JA03637

Balch, C., Murtagh, M., Zezula, D., Combs, L., Nelson, G., Tegnell, K., ... McGehan, B. (2004). Intense Space Weather Storms October 19–November 07, 2003. *United States National Space Weather Service, Service Assessment, 60 pp*. Retrieved from https://repository.library.noaa.gov/view/noaa/6995

Bedrosian, P. A., & Love, J. J. (2015). Mapping geoelectric fields during magnetic storms: Synthetic analysis of empirical United States impedances. *Geophysical Research Letters*, *42*(23), 10160-10170. doi: 10.1002/2015GL066636

Belakhovsky, V., Pilipenko, V., Engebretson, M., Sakharov, Y., & Selivanov, V. (2019). Impulsive disturbances of the geomagnetic field as a cause of induced currents of electric power lines. *Journal of Space Weather and Space Climate*, *9*, A18. doi: 10.1051/swsc/2019015

Chi, P. J., Russell, C. T., Foster, J. C., Moldwin, M. B., Engebretson, M. J., & Mann, I. R. (2005). Density enhancement in plasmasphere-ionosphere plasma during the 2003 Halloween Superstorm: Observations along the 330th magnetic meridian in North America. *Geophysical Research Letters*, *32*(3), L03S07. doi: 10.1029/2004GL021722

Claudepierre, S., Toffoletto, F., & Wiltberger, M. (2016). Global MHD model-

ing of resonant ULF waves: Simulations with and without a plasmasphere. *Journal of Geophysical Research: Space Physics*, *121*(1), 227–244. doi: 10.1002/2015JA022048

Claudepierre, S., Wiltberger, M., Elkington, S., Lotko, W., & Hudson, M. (2009). Magnetospheric cavity modes driven by solar wind dynamic pressure fluctuations. *Geophysical Research Letters*(L13101). doi: 10.1029/2009GL039045

Clilverd, M. A., Rodger, C. J., Brundell, J. B., Dalzell, M., Martin, I., Mac Manus, D. H., ... Obana, Y. (2018). Long-Lasting Geomagnetically Induced Currents and Harmonic Distortion Observed in New Zealand During the 7-8 September 2017 Disturbed Period. *Space Weather*, *16*(6), 704-717. doi: 10.1029/2018SW001822

Clilverd, M. A., Rodger, C. J., Brundell, J. B., Dalzell, M., Martin, I., Mac Manus, D. H., & Thomson, N. R. (2020). Geomagnetically Induced Currents and Harmonic Distortion: High Time Resolution Case Studies. *Space Weather*, *18*(10), e02594. doi: 10.1029/2020SW002594

Emmert, J. T., Richmond, A. D., & Drob, D. P. (2010). A computationally compact representation of Magnetic-Apex and Quasi-Dipole coordinates with smooth base vectors. *Journal of Geophysical Research: Space Physics*, *115*(A8), A08322. doi: 10.1029/2010JA015326

Fujii, I., Ookawa, T., Nagamachi, S., & Owada, T. (2015). The characteristics of geoelectric fields at Kakioka, Kanoya, and Memambetsu inferred from voltage measurements during 2000 to 2011. *Earth, Planets and Space*, *67*. doi: 10.1186/s40623-015-0241-z

Fujita, S., Tanaka, T., Kikuchi, T., Fujimoto, K., & Itonaga, M. (2003). A numerical simulation of the geomagnetic sudden commencement: 2. Plasma processes in the main impulse. *Journal of Geophysical Research: Space Physics*, *108*(A12).

Gjerloev, J. W. (2012). The SuperMAG data processing technique. *Journal of Geophysical Research: Space Physics*, *117*(A9), A09213. doi: 10.1029/2012JA017683

Glassmeier, K.-H., Othmer, C., Cramm, R., Stellmacher, M., & Engebretson, M. (1999). Magnetospheric Field Line Resonances: A Comparative Planetology Approach. *Surveys in Geophysics*, *20*(1), 61-109. doi: 10.1023/A:1006659717963

Grawe, M. A., & Makela, J. J. (2021). Predictability of Geomagnetically Induced Currents as a Function of Available Magnetic Field Information. *Space Weather*, *19*(8), e02747. doi: 10.1029/2021SW002747

Grawe, M. A., Makela, J. J., Butala, M. D., & Kamalabadi, F. (2018). The Impact of Magnetic Field Temporal Sampling on Modeled Surface Electric Fields. *Space Weather*, *16*(11), 1721-1739. doi: 10.1029/2018SW001896

Hapgood, M., Knipp, D. J., & Knipp. (2016). Data Citation and Availability: Striking a Balance Between the Ideal and the Practical. *Space Weather*, *14*(11), 919-920. doi: 10.1002/2016SW001553

Hartinger, M., Plaschke, F., Archer, M., Welling, D., Moldwin, M., & Ridley, A. (2015). The global structure and time evolution of dayside magnetopause surface eigenmodes. *Geophysical Research Letters*, *42*(8), 2594–2602. doi: 10.1002/2015GL063623

Hartinger, M., Welling, D., Viall, N. M., Moldwin, M. B., & Ridley, A. (2014). The effect of magnetopause motion on fast mode resonance. *Journal of Geophysical Research: Space Physics*, *119*(10), 8212–8227. doi: 10.1002/2014JA020401

Hartinger, M. D., Jürgen, M., Petersen, T., & Rodger, C. (2022). Geomagnetic (ngk, eyr) and geoelectric (ngk) field measurements [data set]. *Zenodo*. doi: 10.5281/zenodo.7261515

Hartinger, M. D., Shi, X., Lucas, G. M., Murphy, B. S., Kelbert, A., Baker, J. B. H., ... Bedrosian, P. A. (2020). Simultaneous Observations of Geoelectric and Geomagnetic Fields Produced by Magnetospheric ULF Waves. *Geophysical*

Research Letters, *47*(18), e89441. doi: 10.1029/2020GL089441

Hartinger, M. D., Zou, S., Takahashi, K., Shi, X., Redmon, R., Goldstein, J., ... Bonnell, J. W. (2017). Nightside Pi2 Wave Properties During an Extended Period With Stable Plasmapause Location and Variable Geomagnetic Activity. *Journal of Geophysical Research: Space Physics*, *122*(12), 12120-12139. doi: 10.1002/2017JA024708

Hejda, P., & Bochníček, J. (2005). Geomagnetically induced pipe-to-soil voltages in the Czech oil pipelines during October-November 2003. *Annales Geophysicae*, *23*(9), 3089-3093. doi: 10.5194/angeo-23-3089-2005

Heyns, M. J., Gaunt, C., Lotz, S., & Cilliers, P. J. (2020). Data driven transfer functions and transmission network parameters for GIC modelling. *Electric Power Systems Research*, *188*, 106546. doi: 10.1016/j.epsr.2020.106546

Heyns, M. J., Lotz, S. I., & Gaunt, C. T. (2021). Geomagnetic Pulsations Driving Geomagnetically Induced Currents. *Space Weather*, *19*(2), e02557. doi: 10.1029/2020SW002557

Jacobs, J. A., Kato, Y., Matsushita, S., & Troitskaya, V. A. (1964). Classification of geomagnetic micropulsations. *Journal of Geophysical Research*, *69*(1), 180-181. doi: 10.1029/JZ069i001p00180

Kale, Z. C., Mann, I. R., Waters, C. L., Vellante, M., Zhang, T. L., & Honary, F. (2009). Plasmaspheric dynamics resulting from the Hallowe'en 2003 geomagnetic storms. *Journal of Geophysical Research: Space Physics*, *114*(A8), A08204. doi: 10.1029/2009JA014194

Kappenman, J. G. (2003). Storm sudden commencement events and the associated geomagnetically induced current risks to ground-based systems at low-latitude and midlatitude locations. *Space Weather*, *1*(3), 1016. doi: 10.1029/2003SW000009

Kappenman, J. G. (2005). An overview of the impulsive geomagnetic field disturbances and power grid impacts associated with the violent Sun-Earth connection events of 29-31 October 2003 and a comparative evaluation with other contemporary storms. *Space Weather*, *3*(8), S08C01. doi: 10.1029/2004SW000128

Kappler, K. N., Morrison, H. F., & Egbert, G. D. (2010). Long-term monitoring of ULF electromagnetic fields at Parkfield, California. *Journal of Geophysical Research (Solid Earth)*, *115*(B4), B04406. doi: 10.1029/2009JB006421

Keiling, A., & Takahashi, K. (2011). Review of Pi2 Models. *Space Science Reviews*, *161*(1-4), 63-148. doi: 10.1007/s11214-011-9818-4

Kelbert, A., Balch, C. C., Pulkkinen, A., Egbert, G. D., Love, J. J., Rigler, E. J., & Fujii, I. (2017). Methodology for time-domain estimation of storm time geoelectric fields using the 3-D magnetotelluric response tensors. *Space Weather*, *15*(7), 874-894. doi: 10.1002/2017SW001594

Lee, D.-H., & Takahashi, K. (2006). MHD Eigenmodes in the Inner Magnetosphere. In K. Takahashi, P. Chi, R. Denton, & R. Lysak (Eds.), *Magnetospheric ulf waves: Synthesis and new directions* (Vol. 169, p. 73). American Geophysical Union (AGU). doi: 10.1029/169GM07

Love, J. J., & Chulliat, A. (2013). An international network of magnetic observatories. *Eos*, *94*(42), 3730374. doi: 10.1002/2013EO420001

Love, J. J., & Finn, C. A. (2011). The USGS Geomagnetism Program and Its Role in Space Weather Monitoring. *Space Weather*, *9*(7), 07001. doi: 10.1029/2011SW000684

Love, J. J., & Gannon, J. L. (2010). Movie-maps of low-latitude magnetic storm disturbance. *Space Weather*, *8*(6), 06001. doi: 10.1029/2009SW000518

Love, J. J., Lucas, G. M., Bedrosian, P. A., & Kelbert, A. (2019). Extreme-Value Geoelectric Amplitude and Polarization Across the Northeast United States. *Space Weather*, *17*(3), 379-395. doi: 10.1029/2018SW002068

Lucas, G. M., Love, J. J., & Kelbert, A. (2018). Calculation of Voltages in Electric

Power Transmission Lines During Historic Geomagnetic Storms: An Investigation Using Realistic Earth Impedances. *Space Weather*, *16*(2), 185-195. doi: 10.1002/2017SW001779

Lucas, G. M., Love, J. J., Kelbert, A., Bedrosian, P. A., & Rigler, E. J. (2020). A 100-year Geoelectric Hazard Analysis for the U.S. High-Voltage Power Grid. *Space Weather*, *18*(2), e02329. doi: 10.1029/2019SW002329

Mac Manus, D. H., Rodger, C. J., Dalzell, M., Thomson, A. W., Clilverd, M. A., Petersen, T., ... Divett, T. (2017). Long-term geomagnetically induced current observations in New Zealand: Earth return corrections and geomagnetic field driver. *Space Weather*, *15*(8), 1020–1038. doi: 10.1002/2017SW001635

Marin, J., Pilipenko, V., Kozyreva, O., Stepanova, M., Engebretson, M., Vega, P., & Zesta, E. (2014). Global Pc5 pulsations during strong magnetic storms: excitation mechanisms and equatorward expansion. *Annales Geophysicae*, *32*(4), 319-331. doi: 10.5194/angeo-32-319-2014

Marshall, R., Dalzell, M., Waters, C., Goldthorpe, P., & Smith, E. (2012). Geomagnetically induced currents in the New Zealand power network. *Space Weather*, *10*(S08003). doi: 10.1029/2012SW000806

McPherron, R. L. (2005). Magnetic pulsations: their sources and relation to solar wind and geomagnetic activity. *Surveys in Geophysics*, *26*(5), 545–592. doi: 10.1007/s10712-005-1758-7

Minamoto, Y. (2013). Availability and access to data from Kakioka Magnetic Observatory, Japan. *Data Science Journal*(12), 30-35. doi: 10.2481/dsj.G-040

Ngwira, C. M., Pulkkinen, A., McKinnell, L.-A., & Cilliers, P. J. (2008). Improved modeling of geomagnetically induced currents in the South African power network. *Space Weather*, *6*(11), S11004. doi: 10.1029/2008SW000408

Orr, D. (1973). Magnetic pulsations within the magnetosphere: A review. *Journal of Atmospheric and Terrestrial Physics*, *35*, 1-50. doi: 10.1016/0021-9169(73)90214-6

Oyedokun, D., Heyns, M., Cilliers, P., & Gaunt, C. (2020). Frequency Components of Geomagnetically Induced Currents for Power System Modelling. *2020 International SAUPEC/RobMech/PRASA Conference, Cape Town, South Africa*, 1-6. doi: 10.1109/SAUPEC/RobMech/PRASA48453.2020.9041021

Ozturk, D. S., Zou, S., & Slavin, J. A. (2017). IMF B_y effects on ground magnetometer response to increased solar wind dynamic pressure derived from global MHD simulations. *Journal of Geophysical Research: Space Physics*, *122*(5), 5028-5042. doi: 10.1002/2017JA023903

Panasyuk, M. I., Solar Extreme Events in 2003 Collaboration SEE-2003, Kuznetsov, S. N., Lazutin, L. L., Avdyushin, S. I., Alexeev, I. I., ... Yushkov, B. Y. (2004). Magnetic Storms in October 2003. *Cosmic Research*, *42*(5), 489-535. doi: 10.1023/B:COSM.0000046230.62353.61

Pilipenko, V. (2021). Space weather impact on ground-based technological systems. *Solar-Terrestrial Physics*, *7*(3), 68-104. doi: 10.12737/stp-73202106

Pilipenko, V., Kozyreva, O., Belakhovsky, V., Engebretson, M. J., & Samsonov, S. (2010). Generation of magnetic and particle Pc5 pulsations during the recovery phase of strong magnetic storms. *Proceedings of the Royal Society of London Series A*, *466*(2123), 3363-3390. doi: 10.1098/rspa.2010.0079

Potapov, A., Guglielmi, A., Tsegmed, B., & Kultima, J. (2006). Global Pc5 event during 29 31 October 2003 magnetic storm. *Advances in Space Research*, *38*(8), 1582-1586. doi: 10.1016/j.asr.2006.05.010

Pulkkinen, A., Bernabeu, E., Thomson, A., Viljanen, A., Pirjola, R., Boteler, D., ... MacAlester, M. (2017). Geomagnetically induced currents: Science, engineering, and applications readiness. *Space Weather*, *15*(7), 828-856. doi: 10.1002/2016SW001501

Pulkkinen, A., & Kataoka, R. (2006). S-transform view of geomagnetically induced currents during geomagnetic superstorms. *Geophysical Research Letters*,

33(12), L12108. doi: 10.1029/2006GL025822

Pulkkinen, A., Lindahl, S., Viljanen, A., & Pirjola, R. (2005). Geomagnetic storm of 29-31 October 2003: Geomagnetically induced currents and their relation to problems in the Swedish high-voltage power transmission system. *Space Weather*, *3*(8), S08C03. doi: 10.1029/2004SW000123

Pulkkinen, A., Viljanen, A., & Pirjola, R. (2006). Estimation of geomagnetically induced current levels from different input data. *Space Weather*, *4*(S08005). doi: 10.1029/2006SW000229

Pulkkinen, T., Gombosi, T., Ridley, A., Toth, G., & Zou, S. (2021). The Space Weather Modeling Framework Goes Open Access. *Eos*, *102*. doi: 10.1029/2021EO158300

Rigler, E., & USGS Geomagnetism Program. (2023). One-second usgs magnetic observatory data collected before 2013: U.s. geological survey data release. doi: 10.5066/P91S9DIF

Rodger, C. J., Clilverd, M. A., Mac Manus, D. H., Martin, I., Dalzell, M., Brundell, J. B., ... Watson, N. R. (2020). Geomagnetically Induced Currents and Harmonic Distortion: Storm-Time Observations From New Zealand. *Space Weather*, *18*(3), e02387. doi: 10.1029/2019SW002387

Rodger, C. J., Mac Manus, D. H., Dalzell, M., Thomson, A. W. P., Clarke, E., Petersen, T., ... Divett, T. (2017). Long-Term Geomagnetically Induced Current Observations From New Zealand: Peak Current Estimates for Extreme Geomagnetic Storms. *Space Weather*, *15*(11), 1447-1460. doi: 10.1002/2017SW001691

Rogers, N. C., Wild, J. A., Eastoe, E. F., & Hübert, J. (2021). Climatological Statistics of Extreme Geomagnetic Fluctuations With Periods From 1 s to 60 min. *Space Weather*, *19*(11), e02824. doi: 10.1029/2021SW002824

Rosenqvist, L., Fristedt, T., Dimmock, A. P., Davidsson, P., Fridström, R., Hall, J. O., ... Wintoft, P. (2022). 3D Modeling of Geomagnetically Induced Currents in Sweden - Validation and Extreme Event Analysis. *Space Weather*, *20*(3), e2021SW002988. doi: 10.1029/2021SW002988

Saito, T., & Matsushita, S. (1967). Geomagnetic pulsations associated with sudden commencements and sudden impulses. *Planetary and Space Sciences*, *15*, 573-582. doi: 10.1016/0032-0633(67)90163-8

Shi, X., Baker, J. B. H., Ruohoniemi, J. M., Hartinger, M. D., Frissell, N. A., & Liu, J. (2017). Simultaneous space and ground-based observations of a plasmaspheric virtual resonance. *Journal of Geophysical Research: Space Physics*, *122*(4), 4190-4209. doi: 10.1002/2016JA023583

Shi, X., Hartinger, M. D., Baker, J. B. H., Murphy, B. S., Bedrosian, P. A., Kelbert, A., & Rigler, E. J. (2022). Characteristics and Sources of Intense Geoelectric Fields in the United States: Comparative Analysis of Multiple Geomagnetic Storms. *Space Weather*, *20*(4), e2021SW002967. doi: 10.1029/2021SW002967

Shi, X., Lin, D., Wang, W., Baker, J. B. H., Weygand, J. M., Hartinger, M. D., ... Shepherd, S. G. (2022). Geospace Concussion: Global Reversal of Ionospheric Vertical Plasma Drift in Response to a Sudden Commencement. *Geophysical Research Letters*, *49*(19), e2022GL100014. doi: 10.1029/2022GL100014

Southwood, D. J., & Hughes, W. (1983). Theory of hydromagnetic waves in the magnetosphere. *Space Science Reviews*, *35*(4), 301-366. doi: 10.1007/BF00169231

St. Louis, B. (2020). INTERMAGNET Technical Reference Manual, Version 5.0.0. *GFZ Data Services, Potsdam, 146 pp.*. doi: 10.48440/INTERMAGNET.2020.001

Sugiura, M., & Wilson, C. R. (1964). Oscillation of the Geomagnetic Field Lines and Associated Magnetic Perturbations at Conjugate Points. *Journal of Geophysical Research*, *69*(7), 1211-1216. doi: 10.1029/JZ069i007p01211

Takahashi, K., & Anderson, B. J. (1992). Distribution of ULF energy (f≤80 mHz) in the inner magnetosphere: A statistical analysis of AMPTE CCE magnetic field data. *Journal of Geophysical Research: Space Physics*, *97*(A7), 10751-10773. doi: 10.1029/92JA00328

Takahashi, K., Lee, D.-H., Nosé, M., Anderson, R. R., & Hughes, W. J. (2003). CRRES electric field study of the radial mode structure of Pi2 pulsations. *Journal of Geophysical Research: Space Physics*, *108*(A5), 1210. doi: 10.1029/2002JA009761

Takahashi, K., Lysak, R., Vellante, M., Kletzing, C. A., Hartinger, M. D., & Smith, C. W. (2018). Observation and Numerical Simulation of Cavity Mode Oscillations Excited by an Interplanetary Shock. *Journal of Geophysical Research: Space Physics*, *123*(3), 1969-1988. doi: 10.1002/2017JA024639

Takasaki, S., Kawano, H., Tanaka, Y., Yoshikawa, A., Seto, M., Iizima, M., ... Yumoto, K. (2006). A significant mass density increase during a large magnetic storm in October 2003 obtained by ground-based ULF observations at L∼1.4. *Earth, Planets and Space*, *58*, 617-622. doi: 10.1186/BF03351959

Tamao, T. (1965). Transmission and coupling resonance of hydromagnetic disturbances in the non-uniform Earth's magnetosphere. *Science reports of the Tohoku University. Series 5, Geophysics*, *17*, 43–70.

Tanskanen, E. (2009). A comprehensive high-throughput analysis of substorms observed by IMAGE magnetometer network: Years 1993–2003 examined. *Journal of Geophysical Research: Space Physics*, *114*(A05204). doi: 10.1029/2008JA013682

Thomson, A. W. P. (2007). Geomagnetic hazards. In D. Gubbins & E. Herrero-Bervera (Eds.), *Encyclopedia of geomagnetism and paleomagnetism* (pp. 316–319). Dordrecht: Springer Netherlands. doi: 10.1007/978-1-4020-4423-6_117

Trichtchenko, L. (2021). Frequency Considerations in GIC Applications. *Space Weather*, *19*(8), e02694. doi: 10.1029/2020SW002694

Viljanen, A., Pulkkinen, A., Pirjola, R., Pajunpää, K., Posio, P., & Koistinen, A. (2006). Recordings of geomagnetically induced currents and a nowcasting service of the Finnish natural gas pipeline system. *Space Weather*, *4*(10), S10004. doi: 10.1029/2006SW000234

Wedeken, U., Voelker, H., Knott, K., & Lester, M. (1986). SSC-excited pulsations recorded near noon on GEOS 2 and on the ground (CDAW 6). *Journal of Geophysical Research: Space Physics*, *91*(A3), 3089-3100. doi: 10.1029/JA091iA03p03089

Wild, J. A., Yeoman, T. K., & Waters, C. L. (2005). Revised time-of-flight calculations for high-latitude geomagnetic pulsations using a realistic magnetospheric magnetic field model. *Journal of Geophysical Research: Space Physics*, *110*(A11), A11206. doi: 10.1029/2004JA010964

Wright, A. N., & Mann, I. R. (2006). Global MHD Eigenmodes of the Outer Magnetosphere. In K. Takahashi, P. Chi, R. Denton, & R. Lysak (Eds.), *Magnetospheric ulf waves: Synthesis and new directions* (Vol. 169, p. 51). American Geophysical Union (AGU). doi: 10.1029/169GM06

Yagova, N. V., Pilipenko, V. A., Sakharov, Y. A., & Selivanov, V. N. (2021). Spatial scale of geomagnetic Pc5/Pi3 pulsations as a factor of their efficiency in generation of geomagnetically induced currents. *Earth, Planets and Space*, *73*(1), 88. doi: 10.1186/s40623-021-01407-2

Yu, Y.-Q., & Ridley, A. J. (2011). Understanding the response of the ionosphere-magnetosphere system to sudden solar wind density increases. *Journal of Geophysical Research: Space Physics*, *116*(A4), A04210. doi: 10.1029/2010JA015871

Yumoto, K., Isono, A., Shiokawa, K., Matsuoka, H., Tanaka, Y., Menk, F. W., & Fraser, B. J. (1994). Global cavity mode-like and localized field-line Pc 3-4 oscillations stimulated by interplanetary impulses (Si/Sc): Initial Results

From the 210 MM magnetic observations. In M. Engebretson, K. Takahashi, & M. Scholer (Eds.), *Solar wind sources of magnetospheric ultra low frequency waves* (Vol. 81, p. 335-344). American Geophysical Union (AGU). doi: 10.1029/GM081p0335

Zhang, T., & Ebihara, Y. (2022). Superposed epoch analyses of geoelectric field disturbances in Japan in response to different geomagnetic activities. *Space Weather*, *20*, e2021SW002893. doi: 10.1029/2021SW002893

Figure 1.

Typical ULF Wave Frequencies

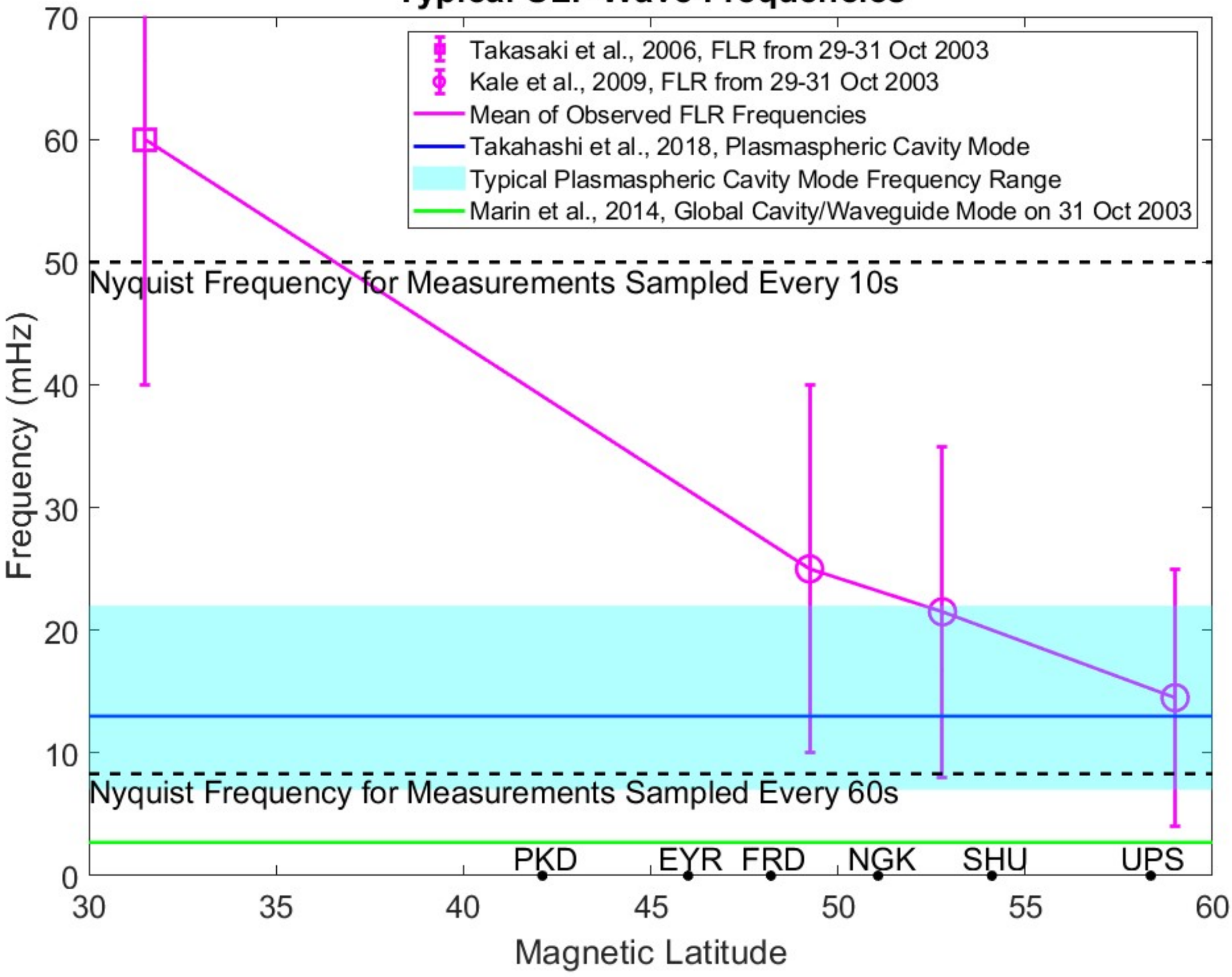

Figure 2.

2003-10-29

A

B

C

D

E

F

G

0.5-10 sec
Intermagnet 1 min
high_pass_filtered
low_pass_filtered
1 min average

PKD_H [nT] FRD_H [nT]
SHU_H [nT]
EYR_H [nT]
KAK_H [nT]
NGK_H [nT] UPS_H [nT]

50
0
−50
100
−100
200

06:05
06:10
06:15
06:20
06:25

Time (UT)

Figure 3.

2003, EYR

A

B

EYR_H [nT]

500
0
−500

100
50
0
−50
−100

1

2

5 sec
low_pass_filtered

high_pass_filtered

00:00
10-29

12:00
10-29

00:00
10-30

12:00
10-30

00:00
10-31

12:00
10-31

00:00
11-01

Time (UT)

2003-10-29, EYR

C

Interval 1

200
0
−200

5 sec
low_pass_filtered
high_pass_filtered

06:00
06:10
06:20
06:30
06:40
06:50
07:00

2003-10-31, EYR

D

Interval 2

200
100
0
−100

5 sec
low_pass_filtered
high_pass_filtered

02:00
02:10
02:20
02:30
02:40
02:50
03:00

Figure 4.

29-31 Oct 2003, EYR dHdt

A

5 sec

low-pass filtered

500

0

-500

nT / min

1

2

B

high-pass filtered

500

0

-500

nT / min

00:00 10-29

00:00 10-30

00:00 10-31

00:00 11-01

Time (UT)

2003-10-29, EYR dHdt

C

5sec

5sec low-pass filtered

INTERMAGNET 60sec

5sec high-pass filtered

500

0

-500

nT / min

Interval 1

06:00

06:05

06:10

06:15

06:20

06:25

06:30

06:35

06:40

06:45

06:50

06:55

07:00

Time (UT)

2003-10-31, EYR dHdt

D

5sec

5sec low-pass filtered

INTERMAGNET 60sec

5sec high-pass filtered

500

0

-500

nT / min

Interval 2

02:00

02:05

02:10

02:15

02:20

02:25

02:30

02:35

02:40

02:45

02:50

02:55

03:00

Time (UT)

Figure 5.

2003-10-29

A
Ex [mV/km]
100
0
PKD 1 sec
low_pass_filtered
high_pass_filtered

B
Ey [mV/km]
10
0
−10
PKD 1 sec
low_pass_filtered
high_pass_filtered

C
Ex [mV/km]
50
0
−50
NGK 1 sec
low_pass_filtered
high_pass_filtered

D
Ey [mV/km]
50
0
NGK 1 sec
low_pass_filtered
high_pass_filtered

E
Ex [mV/km]
0
−100
KAK 1 sec
low_pass_filtered
high_pass_filtered

F
Ey [mV/km]
0
−500
KAK 1 sec
low_pass_filtered
high_pass_filtered

06:05
06:10
06:15
06:20
06:25
Time (UT)

Figure 6.

29-31 Oct 2003, KAK Ey

A

B

mV / km

400
200
0
-200
-400
-600

1

2

1 sec
low-pass filtered

high-pass filtered

00:00 10-29
00:00 10-30
00:00 10-31
00:00 11-01

Time (UT)

2003-10-29, KAK Ey

C

Interval 1

1 sec
1sec low-pass filtered
60 sec low-pass filtered
1sec high-pass filtered

06:00 06:05 06:10 06:15 06:20 06:25 06:30 06:35 06:40 06:45 06:50 06:55 07:00

Time (UT)

2003-10-31, KAK Ey

D

Interval 2

02:00 02:05 02:10 02:15 02:20 02:25 02:30 02:35 02:40 02:45 02:50 02:55 03:00

Time (UT)

Figure 7.

29-31 Oct 2003, EYR dHdt and ISL M6 GIC

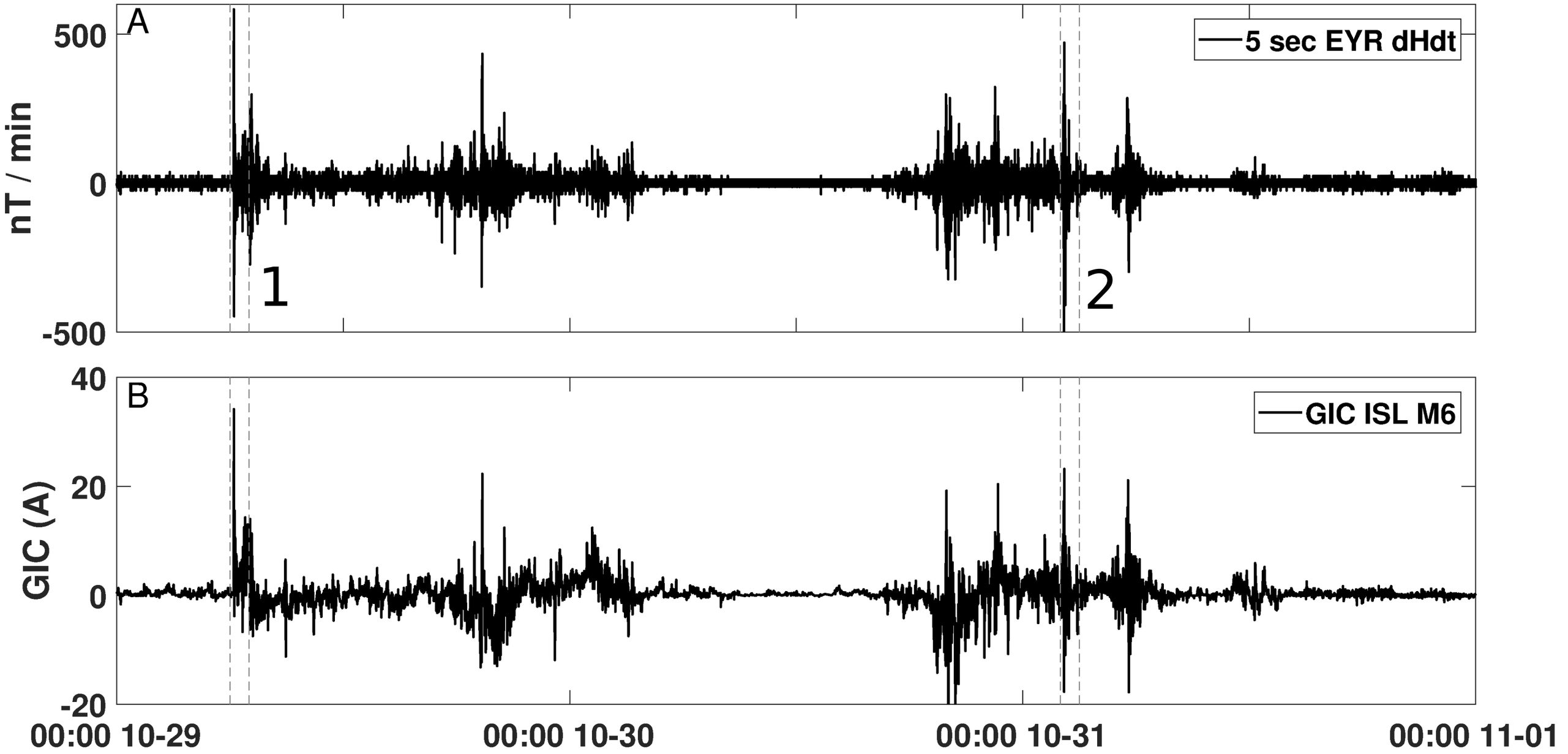

2003-10-29, ISL M6 GIC

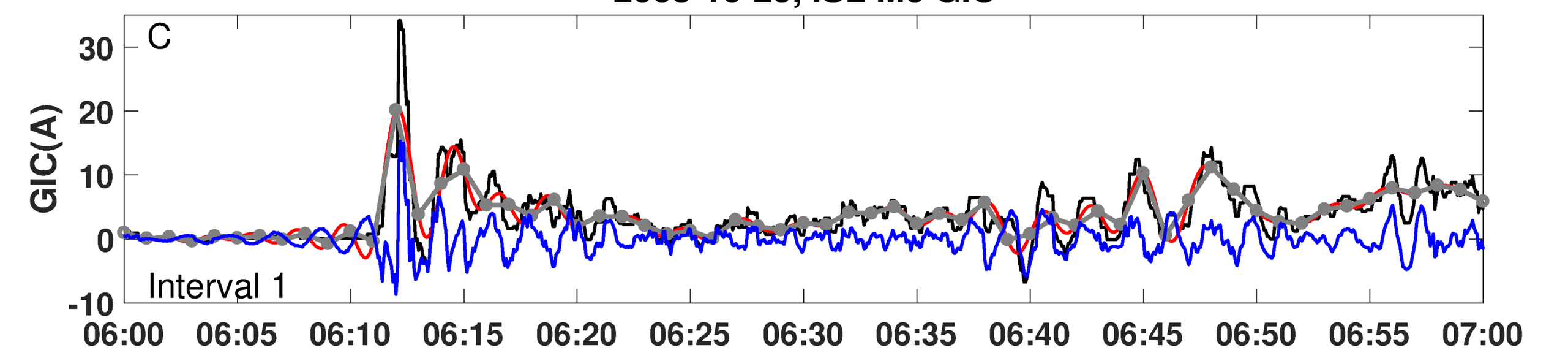

2003-10-31, ISL M6 GIC

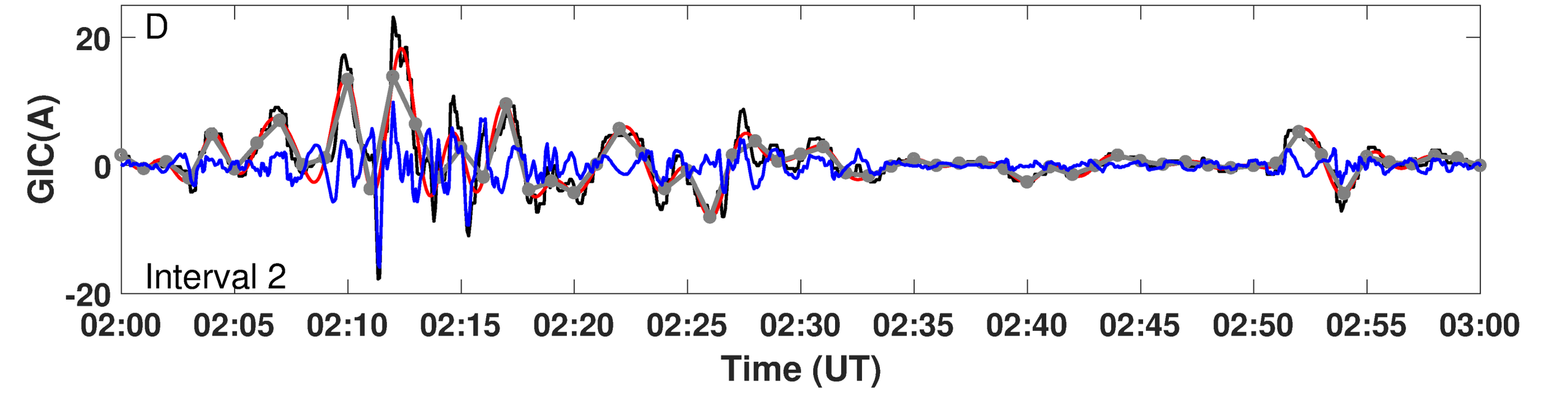

Figure 8.

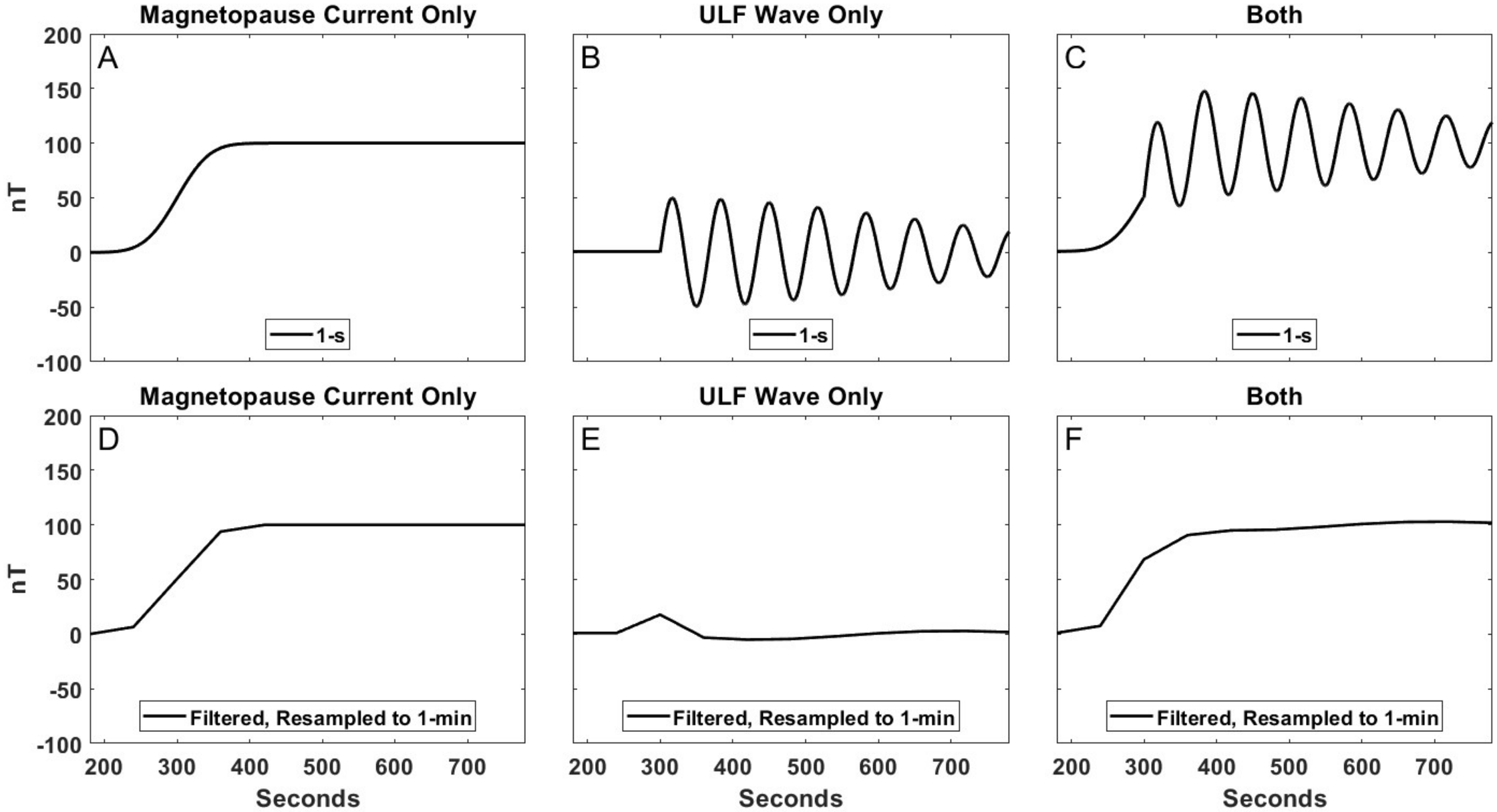
Magnetopause Current Only
ULF Wave Only
Both
A
B
C
D
E
F
nT
200
150
100
50
0
-50
-100
1-s
Filtered, Resampled to 1-min
200
300
400
500
600
700
Seconds